A spatial model of autophosphorylation of Ca^{2+}/calmodulin-dependent protein kinase II in a glutamatergic spine reveals dynamics of kinase activation in the first several seconds after a complex synaptic stimulus.

Short title: Simulation of autophosphorylation of CaMKII in a spine

Thomas M. Bartol*[,1], Mariam Ordyan[1], Terrence J. Sejnowski[1,2], Padmini Rangamani*[,4], Mary B. Kennedy*[,3]

[1] The Salk Institute for Biological Studies, La Jolla, CA

[2] Department of Neurobiology, University of California at San Diego, La Jolla, CA

[3] Department of Biology and Biological Engineering, California Institute of Technology, Pasadena, CA

[4] Department of Mechanical and Aerospace Engineering, University of California San Diego, La Jolla, CA

* Each of these authors contributed equally.

All correspondence can be addressed to kennedym@caltech.edu or bartol@salk.edu

Abstract:

Long-term potentiation (LTP) is a biochemical process in excitatory glutamatergic synapses in the Central Nervous System (CNS). It is initiated by a bout of synaptic activation that is strong enough to contribute to production of an action potential in the axon of the postsynaptic neuron, and it results in an increase in the size of postsynaptic depolarization during subsequent activity. The first step leading to LTP is activation and autophosphorylation of an abundant postsynaptic enzyme, Ca^{2+}/calmodulin-dependent protein kinase II (CaMKII). We use simulation of activation of CaMKII holoenzymes in a realistic spatial model of a spine synapse, created in MCell4, to test three hypotheses about how the autophosphorylation response of CaMKII is shaped during a repeated high-frequency stimulus. First, the simulation results indicate that autophosphorylation of CaMKII does not constitute a bistable switch under biologically realistic conditions. Instead, prolonged autophosphorylation of CaMKII may contribute to a biochemical "kinetic proof-reading" mechanism that controls induction of synaptic plasticity. Second, concentration of CaMKII near the postsynaptic membrane increases the local concentration of kinase activity. However, neither localization nor "Ca^{2+}-calmodulin-trapping (CaM-trapping)" increase the proportion of autophosphorylated subunits in holoenzymes after a complex stimulus, as previously hypothesized. Finally, we show that, as hypothesized, the amplitude of autophosphorylation in the first 30 seconds after a stimulus is extremely sensitive to the level and location of PP1 activity when PP1 is present in biologically accurate amounts. We further show that prolonged steric hindrance of dephosphorylation of CaMKII, caused by CaM-trapping, can increase the amplitude of autophosphorylation after a complex stimulus. These simulation results sharpen our quantitative understanding of the early events leading to LTP at excitatory synapses.

Author Summary:

Neurons in the brain are interconnected in an organized fashion by synapses that transmit neuronal activity from one neuron to another. Most of the billions of neurons in the brain have about 10,000 synapses spread over the neuronal membrane. Information is stored in the brain when the ability of specific synapses to pass along neuronal activity is strengthened resulting in formation of new networks. The increase in strength of a synapse is tightly controlled by the frequency and amplitude of its activity, and by neurohormonal signals, which, in combination, can cause long-lasting biochemical changes at the synapse that underlie learning and memory. Defects in these biochemical pathways cause mental and neurological diseases. To develop treatments, we need to understand the precise choreography of these critical biochemical changes. However, the tiny size of the synaptic compartment makes precise measurements of the biochemical reactions impossible. We have used computer simulation techniques and information gathered from experiments on purified synaptic proteins to simulate, within a single synapse, the choreography of the first biochemical step in synaptic strengthening: activation of the enzyme Ca^{2+}/calmodulin-dependent protein kinase II. Our results provide insights that can be used in future studies to develop treatments for neuronal diseases.

Introduction:

Memories are stored in the brain through creation of new neural networks that are formed by strengthening excitatory glutamatergic synapses between neurons that are activated together during an experience (1-3). Each excitatory pyramidal neuron in the forebrain contains approximately 10,000 excitatory glutamatergic synapses arrayed along several dendrites that reach into the surrounding brain tissue. Most excitatory synapses are made by axons onto dendritic spines, which are small tubular membrane extensions with a bulbous head. Spine synapses are comprised of a release site from a presynaptic axon that makes a specialized synaptic contact with a postsynaptic spine (Fig. 1A). The spine contains highly integrated biochemical machinery that regulates synaptic strength by controlling the size of the spine head and the number of α-amino-3-hydroxy-5-methyl-4-isoxazolepropionic acid (AMPA)-type glutamate receptors (AMPARs) located at the synaptic site (4-7).

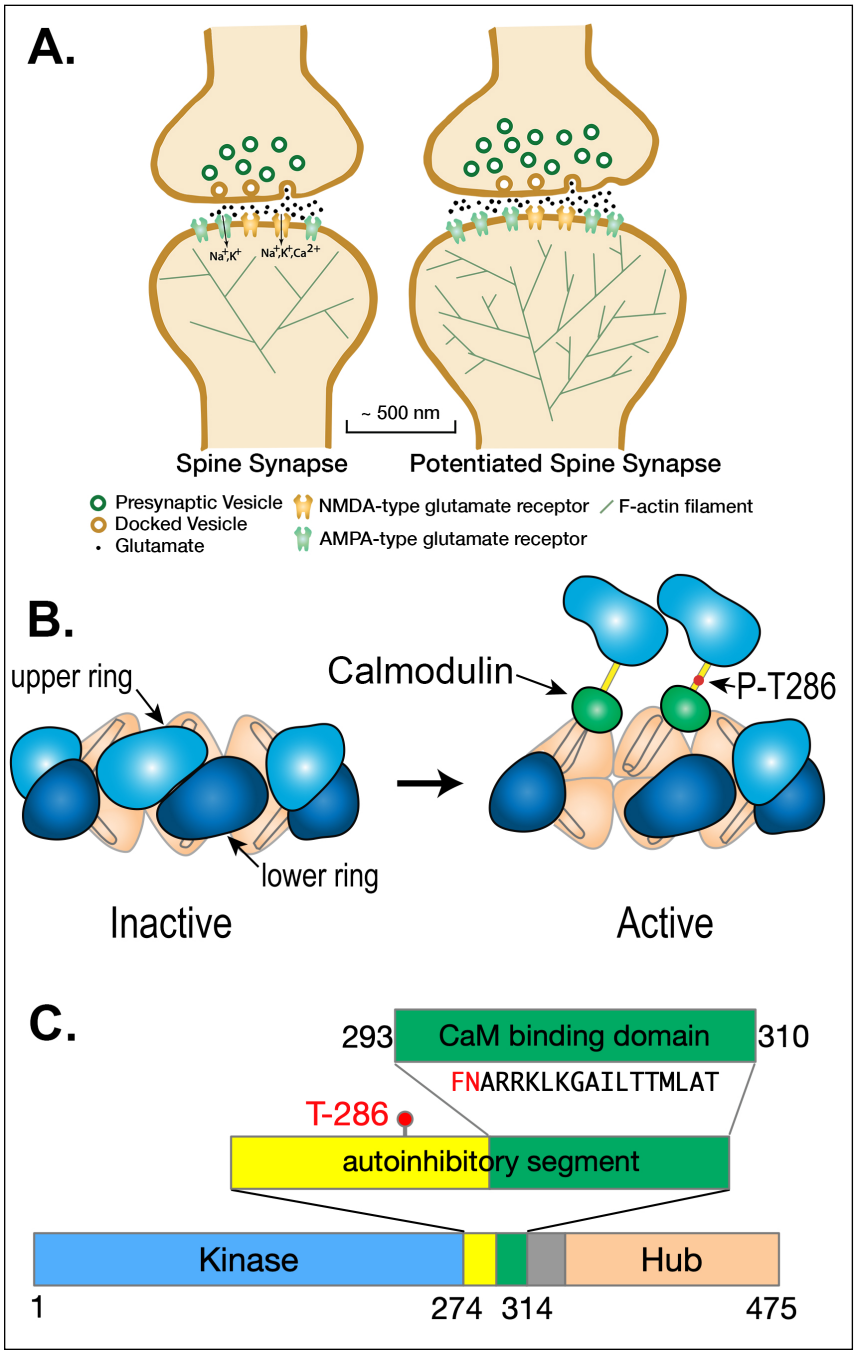

Activation of N-methyl-D-aspartate-type glutamate receptors (NMDARs) at synapses in the CNS triggers changes in synaptic strength that underlie memory formation in response to strong synaptic stimuli (8, 9). Precise kinetic control of this machinery determines the amplitude of changes in synaptic strength that are the basis of new neural networks.

Spine synapses and LTP. Spines are, on average, ~1-2 μm in length. The diameters of spine heads are highly variable, as are their volumes (10, 11, see 12). The median volume of spines in stratum radiatum of hippocampal area CA1 (the source of our model spine) is ~0.017 μm^3 or ~17 x 10^{-18} liters (11). The synaptic membrane contacts between axon release sites and spines are roughly circular and their median diameter is ~200 nm (11). The presynaptic side of the contact contains sites at which vesicles dock at the membrane and release glutamate when the axon is depolarized. The postsynaptic contact is undergirded by the postsynaptic density (PSD), which immobilizes the synaptic receptors for glutamate and anchors a dense network of cytosolic regulatory proteins attached to the membrane (7, 10, 13). The strength of a synapse is highly correlated with the volume of the spine head, as well as the area of the PSD and presynaptic active zone (14). Larger spine heads contain more AMPA-type glutamate receptors and a larger PSD. Thus, they exhibit a larger excitatory postsynaptic potential when glutamate is released from the presynapse (11).

The regulatory biochemical machinery in spines is capable of responding to the frequency of synaptic activation by strengthening (enlarging) or weakening (shrinking) the synapse (6, 15). The biochemical mechanisms that allow the frequency of presynaptic activity to be translated precisely into synaptic strengthening or weakening that faithfully encodes memories is still incompletely understood. The reactions that lead to functional and structural changes in spines are triggered by Ca^{2+} entering the spine through the ion channels of NMDA-type glutamate receptors (NMDARs)

Figure 1. **A**. Schematic diagram of a spine synapse. AMPA-type glutamate receptors (AMPARs, teal) produce a depolarizing Na^+/K^+ current after binding glutamate released from presynaptic vesicles upon arrival of an axonal action potential (AP). NMDA-type glutamate receptors (NMDARs, gold) contain a channel that is opened by the concurrence of glutamate release and strong depolarization (e.g. a back-propagating action potential [bAP]). Potentiated synapses (right) contain more AMPARs resulting in a larger excitatory postsynaptic potential (EPSP) upon release of glutamate. The spines of potentiated synapses increase in size and contain a more highly branched actin cytoskeleton. **B**. Ca^{2+}/calmodulin-dependent protein kinase II (CaMKII) is a dodecameric holoenzyme in which twelve subunits are bound together by the interactions among the hub domains of each subunit. When Ca^{2+}/calmodulin (Ca^{2+}/CaM) binds to two adjacent subunits in one of the hexameric rings, a threonine residue (Thr286) within one of the two subunits is autophosphorylated by the other subunit acting as a kinase. Autophosphorylation is believed to occur in one direction around the hexameric ring. Autophosphorylation of Thr 286 causes the subunit to remain active even when the Ca^{2+} concentration falls and calmodulin (CaM) unbinds. (modified from Fig. 7 of Rosenberg et al. (16). **C**. Domain diagram of a subunit of CaMKII illustrating the catalytic domain (Kinase), the autoinhibitory segment with the CaM-binding domain, and the Hub domain. When the kinase is inactive, the inhibitory segment lies within the site that binds ATP and protein substrates. Binding of Ca^{2+}/CaM to the CaM-binding domain moves the inhibitory segment out of the substrate-binding pocket allowing ATP to bind to the subunit. Thr-286, which can be autophosphorylated, as described in B), is contained within the autoinhibitory segment. Autophosphorylation unmasks a phenylalanine (F) and a glutamine (N) in the CaM-binding domain (shown in red), enabling a large increase in the affinity of Ca^{2+}/CaM, known as CaM-trapping.

(Fig. 1A). Physiological studies show that these functional and structural changes are exquisitely tightly regulated by the frequency and amplitude of Ca^{2+} entry (17, 18).

The principal target of Ca^{2+} entering the spines of cortical and hippocampal excitatory synapses is Ca^{2+}/calmodulin-dependent protein kinase II (CaMKII), which, as its name suggests, is activated when it binds Ca^{2+}-bound calmodulin (Ca^{2+}/CaM) formed when the concentration of Ca^{2+} rises above its baseline value (~100 nM, 19) (Fig. 1B). Activation of CaMKII has been shown to play a crucial role in long term potentiation (LTP) of excitatory synaptic strength in the hippocampus, and therefore in spatial

learning and memory (20, 21). The regulation of CaMKII by Ca^{2+}/CaM has also been studied extensively *in vitro* (19, 22-25). Activated CaMKII subunits within the holoenzyme become autophosphorylated at Thr 286 within the first several seconds of Ca^{2+} influx, eventually enabling binding of subunits to the GluN2B subunit of the NMDAR (26, 27), and to phosphorylation of several additional synaptic proteins (28-31). These events set in motion a cascade of reactions that lead to changes in synaptic strength the magnitude of which depend on the frequency of presynaptic action potentials (APs) and the presence of other regulatory modulators that can influence the sensitivity of the synapse to plastic changes (4, 6, 32).

Modeling of the dynamics of synaptic mechanisms, including activation of CaMKII, has been carried out at different levels of abstraction and mechanistic realism to address a range of different questions. Previous attempts have relied on simplifications of complex spatial mechanisms, often including coarse-grained variables to represent a series of linked mechanisms over several time scales, and/or deterministic compartmental models that rely on differential equations assuming well-mixed conditions in linked small compartments (33, e.g. 34). However, the biochemical reactions that initiate synaptic plasticity *in vivo* occur within small spines containing small numbers of spatially-organized signaling proteins; thus, they satisfy neither the continuum nor the "well-mixed" assumptions required for the use of deterministic methods to model the dynamics of mechanisms. Differential equations can provide estimates of the average dynamics of sets of reactions, but are unable to provide insight into individual mechanisms that are driven *in vivo* by the fluctuating, probabilistic Ca^{2+} signals that arise in the spine at baseline and during synaptic activity.

In one previous hypothesis-driven modeling study (35), the authors searched for parameters that would be compatible with the popular notion of a stimulus-dependent "bistable" switch that would

outlast molecular turnover, composed of CaMKII and the phosphatase PP1 (e.g. 36). However, the parameter ranges they identified are not consistent with data regarding the concentrations of these proteins in synaptic spines.

Here we have tested several assumptions about the kinetics of autophosphorylation of CaMKII using an unbiased data-driven computational model of the dynamics of the principal biochemical mechanisms in the spine that are believed to initiate plasticity. We modeled activation of CaMKII after a complex presynaptic stimulus delivered to a realistic spine synapse. To do this, we have integrated and updated four previous well-tested models to enable us to simulate the activation of dodecameric holoenzymes of CaMKII in a median-sized spine. As described below, the previous models include a model of presynaptic release of glutamate from a CNS synapse (37), a model of Ca^{2+} influx through NMDAR's and L-type Ca^{2+} channels followed by recovery in reconstructed hippocampal postsynaptic spines and dendrites (12), a model of activation of CaMKII subunits by Ca^{2+}/CaM (19), and a model of autophosphorylation of the dodecameric CaMKII holoenzyme (38). We have not attempted to model here the full range of influences that regulate CaMKII activity in the spine synapse because such an analysis will require several manuscripts of this size; rather we present an initial model that provides first-order quantitative information about how the CaMKII holoenzyme in a spine would respond during the first 10-20 seconds of activation of NMDARs by a complex stimulus. In future studies, we will be able to add additional elements in a step-by-step fashion to determine how they influence the dynamics of activation of CaMKII (e.g. 38, 39), downstream binding to other proteins, including GluN2B (26, 27), and its action on enzymatic targets (e.g. 40, 41). Our ultimate goal is to elucidate precise biochemical mechanisms that initiate plasticity by simulating the exact kinetics of the intricate reactions triggered in the first several seconds by Ca^{2+} influx through NMDARs.

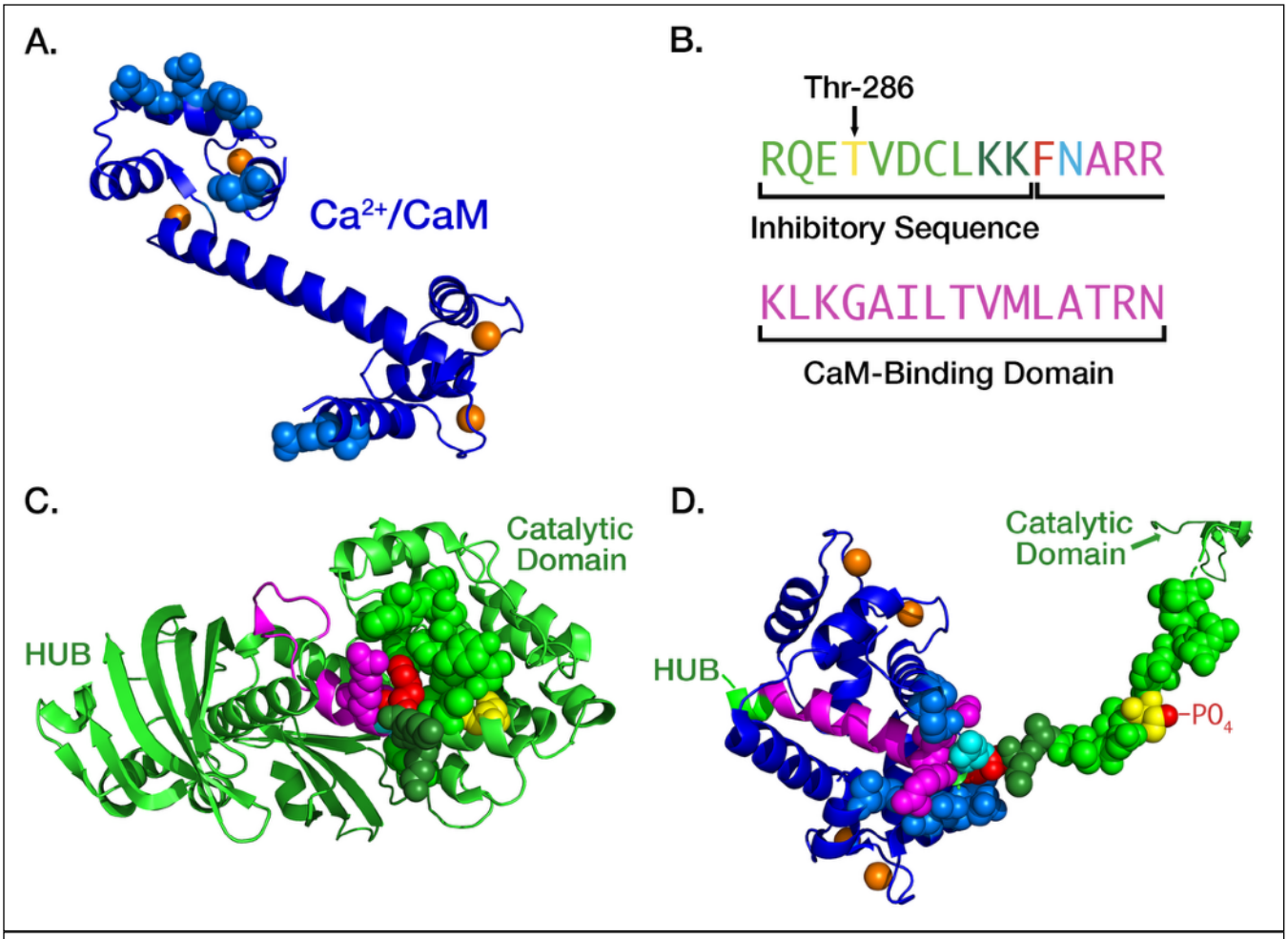

Figure 2. **A**. Ribbon diagram of the atomic structure of CaM with four bound Ca^{2+} ions (orange), two each at its N- and C- termini. The atoms of residues that are bound tightly to the inhibitory segment of CaMKII during trapping are represented as spheres. Rendered in PyMol from pdb #1CLL; **B**. Color-coding of residues comprising the inhibitory and CaM-binding domains of CaMKII subunits: Thr 286 (yellow), two K residues shielding the F and N residues (dark green), F (red), N (cyan), initial CaM-binding domain (magenta). **C**. Ribbon diagram of the atomic structure of an autoinhibited subunit of CaMKII (light green) with the atoms of residues that mask the CaM-trapping amino acids phenylalanine (F, red) and asparagine (N, cyan) shown as light and dark green spheres. Rendered in PyMol from pdb #3SOA; **D**. Ribbon diagram of "trapped" CaM bound to the extended CaM-binding domain. After autophosphorylation of Thr-286 the inhibitory segment assumes a fully extended conformation. The critical F and N residues are exposed and residues on both the N- and C-termini of CaM (blue) bind tightly around the FNARRK portion of the CaM binding domain. Rendered in PyMol from pdb #2WEL.

Medical Relevance. The findings will have medical relevance. Several intractable mental and neurological illnesses, including Alzheimer's disease (42), involve disruptions ("derangements") in mechanisms of synaptic regulation (43, 44). Some of these "derangements" are likely to involve relatively subtle, but devastating, changes in the timing of synaptic reactions. Given the central role of CaMKII activation for synaptic plasticity, it is important to understand the detailed biochemical dynamics of the Ca^{2+}-CaM-CaMKII signaling axis within spines to inform the design of new therapeutics to treat these illnesses.

Structure of CaMKII. CaMKII is a dodecameric holoenzyme comprised of twelve individual catalytic subunits that are organized via their "hub" domains into two hexameric rings stacked together (16; Fig. 1B, C, 45, 46). The kinase activity of each subunit is activated independently by binding of Ca^{2+}/CaM to its CaM-binding domain, which moves the inhibitory domain away from the catalytic pocket and thus activates kinase activity (47). In addition, the subunits can undergo autophosphorylation in which an active subunit phosphorylates a specific threonine residue (Thr 286) within its neighboring subunit if that subunit also has Ca^{2+}/CaM bound to it (22, 48-51). Phosphorylation of Thr 286 blocks inhibition by the regulatory domain (47); therefore, each autophosphorylated subunit stays active as long as Thr 286 remains phosphorylated, and can, in turn, phosphorylate and activate its neighboring subunit when the neighbor binds Ca^{2+}/CaM. Thr 286 can be dephosphorylated by either of two broad-specificity protein phosphatases, phosphatase 1 (PP1) or -2a (PP2a); however, PP1 activity predominates in spines (52-57).

In an important study, Meyer and Schulman (23) found that the initial binding of Ca^{2+}/CaM to a CaMKII subunit occurs with moderate affinity (K_D = ~50 nM). However, the movement of the inhibitory segment caused by autophosphorylation substantially increases the affinity for Ca^{2+}/CaM, a

process they referred to as CaM-trapping. Putkey and Waxham (58) later found that the off-rate of CaM is increased from 6.6 s^{-1} to $9x10^{-5}$ s^{-1}, producing an ~70,000-fold increase in affinity (K_D = ~1.8 pM). Tse et al. (59) showed that autophosphorylation exposes residues Phe293 and Asn294 in the CaM-binding domain, and these residues mediate the high affinity CaM-trapping. After autophosphorylation, residues on both the N- and C-termini of CaM (Fig. 2A) bind tightly around the FNARRK sequence in the CaM-binding domain (Fig. 1C, Fig. 2).

Various investigators have postulated that CaM-trapping leads to an enhanced non-linear increase in autophosphorylation of CaMKII during high frequency synaptic stimulation (9, 60, 61). The tiny spatial compartment of the spine, and the low copy numbers of molecules therein make it impossible to measure enzyme activity experimentally within spine compartments without significantly perturbing the kinetics of protein-protein interactions. However, computational models have the advantage of allowing tests of the importance of individual components of the model, by variation of the parameters and assumptions built into it. In this initial model, we have considered how CaM-trapping will affect the response of CaMKII holoenzymes in a median sized spine to two 1 sec bursts of 50 Hz presynaptic stimulation, spaced 2 sec apart. Under these initial conditions, we show that CaM-trapping does not influence the proportion of autophosphorylation of CaMKII during the intermediate-strength two-epoch stimulus because it doesn't increase binding of CaM to non-phosphorylated subunits, and therefore doesn't increase the probability of new autophosphorylation during the second stimulus epoch. This is the case whether the holoenzymes are distributed uniformly through the spine or concentrated within the PSD.

Consistent with the sensitivity of induction of LTP to activation of PP1 that is observed experimentally (53, 62), we find that the level of autophosphorylation is highly sensitive to small

variations in PP1 activity within the range of the experimentally measured physiological levels that we used in our model. We further find that CaM-trapping may regulate dephosphorylation of CaMKII by prolonging steric hindrance of binding of protein phosphatase-1 (PP1) (see 63).

Model development:

MCell 4 Platform. The models are built with the updated agent-based modeling platform MCell4 (64) which integrates the rule-based, network-free simulation framework of BioNetGen (65) with the spatial simulation capabilities of MCell (66, 67). This version builds on the earlier MCell-R, which employed the reaction methods of NFsim originally developed as a non-spatial simulation platform to read and compute simulations written in the model specification language BNGL (68). NFsim's library of functions carries out the graph operations required for efficient network-free simulation in a spatial context. Thus, it avoids the need to pre-compute a full reaction network and store each possible state in memory. Instead, it executes each rule as needed. The number of rules specified in BNGL is usually much lower than the number of possible reactions in the full network; thus, memory savings are substantial (67). MCell4 improves upon the performance and generality of MCell-R by replacing the NFsim library with a newly developed library of functions, called libBNG, which implements full integration of network-free BNGL directly in MCell. The number of possible reactions of the CaMKII holoenzyme described below would be computationally intractable in other modeling platforms. A Python API was added to MCell4 enabling the model presented here by permitting customizations to the configurations of molecules and reactions that are not easily encoded in CellBlender, the graphical user interface for MCell (69).

Presynaptic Stimulus. We used a stimulus consisting of two epochs of presynaptic action potentials. Each epoch consisted of five bursts of action potentials (APs) delivered sequentially at 5 Hz (e.g. 5

bursts per sec). Each burst contained 5 action potentials delivered at 50 Hz (e.g. 5 APs per 100 msec). The two epochs were separated by 2 sec (Fig. S1 A, B).

Glutamate Release. The time series of glutamate release from the presynaptic terminal during the stimulus were simulated based upon our previous model of presynaptic vesicle release (37, 70). The model of release includes 37 measured parameters, adjusted to 34 degrees C. The model was verified against published experimental studies including: 1) the time course of change of release probability after a single AP (71); 2) magnitude and time course of paired-pulse facilitation (72); and 3) time course of recovery of the release probability after vesicle depletion (70).

A set of 50 realistic stochastic timings of release of glutamate from presynaptic vesicles driven by the two-epoch stimulus were computed in MCell initiated by 50 random seeds. The timings of glutamate release computed in this model took into account stochastic short term plasticity of vesicle fusion, including facilitation by residual Ca^{2+} and depression due to depletion of docked vesicles and resulting decreases in release probability. We assumed a median vesicle size containing 1500 molecules of glutamate (See Fig. 6 in Ref. 73). Releases did not occur with each of the 50 simulated presynaptic APs because for this median-sized spine we simulated the initial release probability as ~0.2. The active zone initially contained 7 docked vesicles. Release was facilitated after the first few stimuli (due to residual presynaptic Ca^{2+} in the active zone) and then depressed due to the reduction in the number of docked vesicles. Simulations initiated by each seed resulted in different stochastic trains of release times. Empty vesicle docking sites were reoccupied with a time constant of 5 seconds (i.e. 0.2 per second rate of redocking per site).

The precise timing of the Glu release after a presynaptic AP was stochastic and sometimes occurred 10's of ms after the AP, especially after a long train of stimuli when the [Ca^{2+}] in the presynaptic

terminal was high (Fig. S1 C, D). If the vesicle docking sites were highly depleted and [Ca^{2+}] was elevated in the terminal, a vesicle sometimes appeared to release "spontaneously" at the moment it docked. The sets of timings of glutamate release were indexed by their seed numbers and used to measure glutamate concentration in the cleft as described below. The release timings for each seed were stored in files and used in the python script, “glu_dependent_rates.py.”

Concentration of glutamate in the cleft. We used used the full spatial model of hippocampal neuropil described in (12) to measure the time course of glutamate concentration in the synaptic cleft at the location of the cluster of 15 NMDA receptors (see below). We assumed release of 1500 molecules of Glu from each vesicle and also assumed that the vesicle release sites were located over the NMDAR cluster. This latter assumption meant that these calculations did not reflect the small variability in glutamate concentration at the NMDARs that would result from stochastic locations of release sites. To measure the glutamate concentration, a measurement box was positioned in the cleft covering the extracellular domains of the receptors. The box was transparent to the diffusion of glutamate. Its depth was equal to the height of the cleft and the sides of the box enclosed the NMDAR cluster. The time course of concentration of glutamate within the box was recorded for each release. Each transient of glutamate in the box was brief with a τ of about 1.2 µs, and had the same peak concentration, ~70 mM, because we did not model a distribution of synaptic vesicle sizes. This concentration time course was used to create a pseudo-first order approximation of binding of glutamate to NMDARs, as follows. If k_{plus} is the second order rate constant for glutamate binding to NMDARs, the rate of binding of glutamate is given by [glu] x [NMDAR] x k_{plus}. Binding of glutamate to each NMDAR in MCell was specified as a first-order transition from an unbound NMDAR to an NMDAR with bound glutamate. The measured time course of the glutamate concentration was used to compute pseudo-first order rate

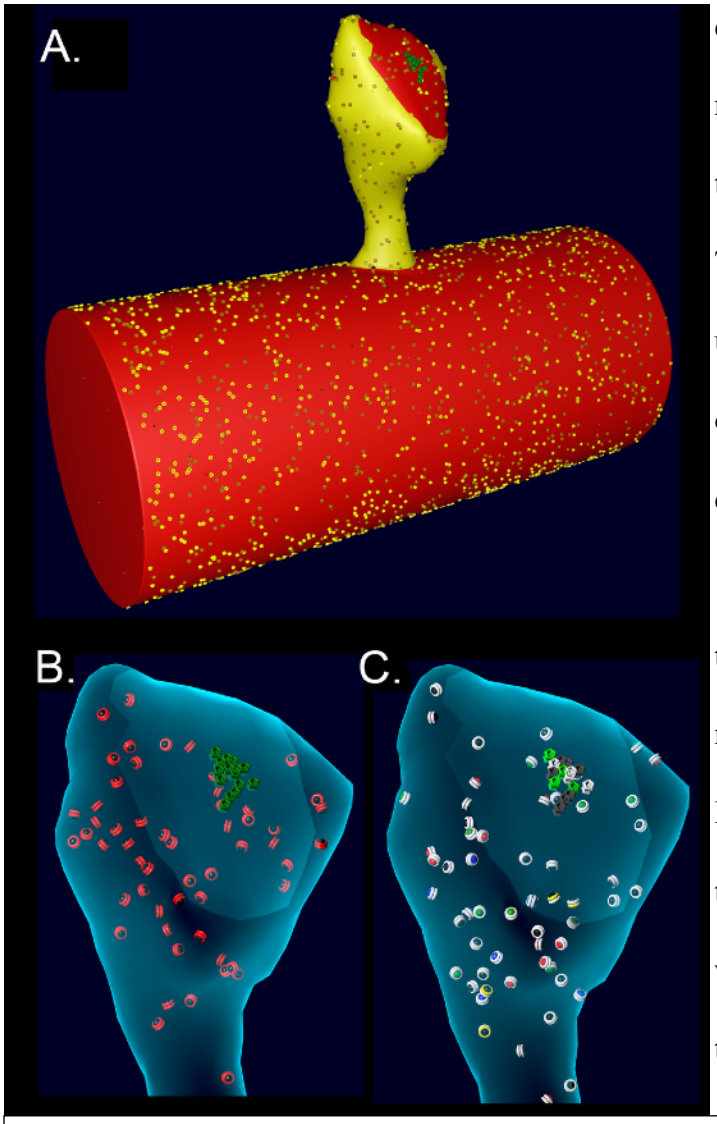

constants, k_{plus}-effective = [glu] x k_{plus}, for each release event and for each seed, as specified in the python script, "glu_dependent_rates.py." The time courses of k_{plus}-effective were then used to determine the probabilities of transition of each NMDAR to the bound state for each seed during the simulation.

NMDAR Response and Ca^{2+} Handling in the Spine. The response of NMDARs was modeled with the kinetics used in our earlier MCell model of Ca^{2+} influx into the spine through NMDARs (12, 74). The spine model was originally constructed with MCell3 within the geometry of a hippocampal dendrite

Figure 3. A. Spine # 37 from (Bartol et al., 2015b) attached to a cylinder with visible glyphs representing surface proteins. The PSD area on the spine and the attached cylinder are shown in red. **B**. A translucent view of spine #37 at instantiation showing surface NMDARs (green) and internal inactive CaMKII holoenzymes (red glyphs). **C**. Spine #37 at t=159 msecs after the start of a stimulus. Open NMDARs on the surface are represented as white glyphs The outer rings of the CaMKII glyphs have changed color to white indicating where CaM with 4 bound Ca^{2+} ions has bound to the subunits (see Results). The color of the internal spheres in the glyphs indicates the number of autophosphorylated subunits in each ring.

reconstructed from serial sections of a 6 x 6 x 5 µm cube of neuropil imaged by electron microscopy (12). The model includes all of the major sources and sinks of Ca^{2+} ion known to be present in the

membranes and cytosol of spines and dendrites. It incorporates experimentally measured kinetics of Ca^{2+} influx through Ca^{2+} channels and NMDARs, including desensitization and the flickering removal of the Mg^{2+} block by a back-propagating action potential. It also includes experimentally measured parameters of Ca^{2+} buffering, and Ca^{2+} removal from the spine via Ca^{2+} exchangers, pumps, and diffusion. Most of the 85 parameters in the model were taken from experimental literature; some were derived from the thermodynamic requirement for microscopic reversibility. All parameters were adjusted to a temperature of 34-37° C. Predicted Ca^{2+} fluxes induced by excitatory postsynaptic potentials (EPSPs) and back-propagating action potentials (bAP's) simulated in the model were validated against an experimental study by Sabatini et al. (75). For the model presented here, one cluster of 15 NMDARs (Fig. 3) was added near the center of the PSD on the reconstructed spine membrane, reflecting recent data about the number and arrangement of NMDARs in hippocampal synapses (e.g. 76, 77).

Spine Geometry. To create an accurate model of the response of CaMKII to Ca^{2+} influx inside a spine, while also minimizing computational time, we imported the geometry of a median-sized spine (#37) from the reconstruction in Bartol et al. (12) and attached it to a cylinder 0.7 μm in diameter and 1.5 μm long, created in Blender (Fig. 3). The wall of the spine has the shape of the inner membrane leaflet, and is reflective to all the volume molecules. The mesh representing the attachment of the spine to the cylinder was adjusted to make it free of leaks (i.e. "water-tight"). The volume of the cytosol of the spine is 0.016 μm^3 (0.016 fl) and the PSD diameter is ~200 nm. The cylinder and spine are instantiated with the appropriate numbers of Ca^{2+} pumps and channels (NCX, PMCA, VDCC) in the membrane, and with cytosolic molecules Ca^{2+}, calbindin, and immobile buffers, as described for the spine and dendritic shaft in (12). We added CaMKII holoenzymes to the cytosol of the spine, encoded as described below, at a concentration of 6.67 μM (60 holoenzymes); thus, individual subunits were present

at a concentration of 80 μM (720 subunits, 45, 78). PP1 was added to the spine cytosol at a "baseline" concentration of 1.25 μM (12 molecules, 79). The k_cat for PP1 was set to 11.5/sec (54) and the K_M for binding to CaMKII was 11 μM (80). Dephosphorylation was modeled as a Michaelis/Menten reaction (see Parameter Table in Supplementary Methods). CaM was added to the cytosol of both the spine and the cylinder at a concentration of 30 μM (81, 82), which is 290 CaM molecules in the spine and ~10,300 in the cylinder. For studies of the effect of phosphatase on autophosphorylation, the concentration of PP1 in the spine was varied from 0.65 μM to 5 μM. Details of the calculations of numbers of CaMKII, CaM, and PP1 are in Supplemental Methods.

Boundary Conditions. In the previous model (12), the spines were attached to a reconstructed dendrite. Diffusing molecules, including Ca^{2+} and calbindin, moved freely through the neck between the spine and the dendritic cytoplasm. The VDCCs, PMCAs, and NCXs in the dendritic membrane contributed to the decay time of the spine Ca^{2+} transient. In that model, we showed that in the first 100 msecs after a stimulus, approximately half of the Ca^{2+} entering spine #37 after an EPSP followed by a bAP exited by diffusion through the neck, either free or bound to calbindin. Thus, in the model presented here, we created appropriate boundary conditions between the neck of the spine and the cylinder. We encased the spine in a shell constructed at a uniform distance of 20 nm from the spine membrane. The shell cuts through the interface at the junction between the spine and the cylinder so that it forms a closed barrier at the base of the spine neck. CaMKII holoenzymes and PP1 are confined to the spine by making this shell reflective to CaMKII and PP1, but transparent to diffusing Ca^{2+}, calmodulin, and calbindin. The length of the cylinder was enlarged until the results of simulations of activation of CaMKII converged when we enlarged it further. Convergence was achieved between cylinder lengths of

A.

CaMKII(r!1,l!6,c!13,T286~0,pp1~0,T306~0,cam~la).CaMKII(r!2,l!1,c!14,T286~0,pp1~0,T306~0,cam~la).
CaMKII(r!3,l!2,c!15,T286~0,pp1~0,T306~0,cam~la).CaMKII(r!4,l!3,c!16,T286~0,pp1~0,T306~0,cam~la).
CaMKII(r!5,l!4,c!17,T286~0,pp1~0,T306~0,cam~la).CaMKII(r!6,l!5,c!18,T286~0,pp1~0,T306~0,cam~la).
CaMKII(r!7,l!12,c!13,T286~0,pp1~0,T306~0,cam~la).CaMKII(r!8,l!7,c!14,T286~0,pp1~0,T306~0,cam~la).
CaMKII(r!9,l!8,c!15,T286~0,pp1~0,T306~0,cam~la).CaMKII(r!10,l!9,c!16,T286~0,pp1~0,T306~0,cam~la).
CaMKII(r!11,l!10,c!17,T286~0,pp1~0,T306~0,cam~la).CaMKII(r!12,l!11,c!18,T286~0,pp1~0,T306~0,cam~la)

B.

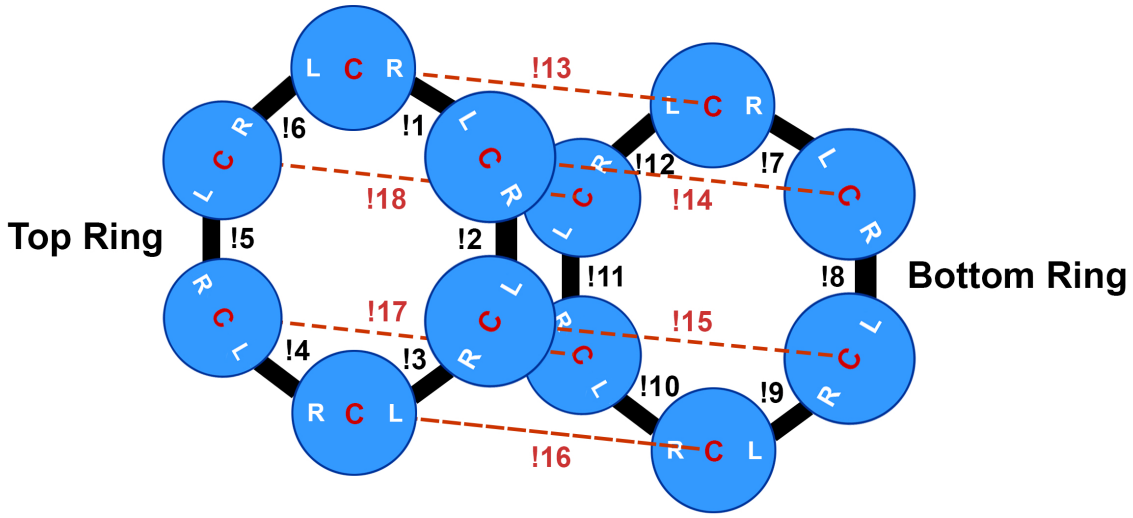

Figure 4. BNGL model of the CaMKII holoenzyme. **A.** The BNGL code represents a CaMKII holoenzyme as it is initialized in a simulation. A single subunit is defined in BNGL as follows (see Ordyan et al., 2020): CaMKII(r,l,c,T286~0~P, pp1~0~1,T306~0~P,cam~la~ha. Components r, l ,and c represent binding sites among subunits in the holoenzyme as diagrammed in **B.** T286 is a component representing the autophosphorylation site threonine-286 which can be present in one of two states ~0 (unphosphorylated) or ~P (phosphorylated). Pp1 is a site for binding of protein phosphatase-1 which can be either unbound (~0) or bound to PP-1 (~1). T306 is the autophosphorylation site threonine-306. Cam represents the binding site for Ca^{2+}/CaM which is allowed to be in either a low affinity binding-state (~la) with K_D = 65 nM or the high affinity state associated with CaM-trapping (~ha) with K_D = 1.8 pM. Bonded subunits are separated by a period. Bonds between components of subunits are represented by the symbol ! (bang) followed by a number. The number must agree for the two components that are bound to each other. The holoenzyme is initialized with no sites phosphorylated and all cam components in the ~la state. B. Diagram of the bonds formed among the r, l , and c sites on each subunit to encode the dodecameric holoenzyme.

1.5 and 1.8 µm. Therefore, the length of the cylinder was set at 1.5 µm, ensuring that the cylinder provides a boundary equivalent to the dendritic shaft.

Calmodulin. The model of initial binding interactions among Ca^{2+}, calmodulin, and individual subunits of CaMKII was based upon our previous non-spatial model of the dynamics of activation of monomeric CaMKII subunits by Ca^{2+}/CaM as the concentration of Ca^{2+} rises (19). This model was created in Mathematica and includes states of Ca^{2+}/CaM with one, two, three, or four bound Ca^{2+} ions. The 55 parameters for Ca^{2+} binding to free CaM and for Ca^{2+} binding to CaM bound to CaMKII were measured experimentally at 30° C by various investigators, including the Kennedy lab (83), or were calculated from the measured parameters using the thermodynamic requirement for microscopic reversibility, involving "detailed balance" of ΔG within reaction loops (see 19).

In the present model, the CaM molecule was encoded in BNGL as follows: CaM(C~0~1~2, N~0~1~2, camkii). In BNGL syntax, the name of the molecule is followed in parentheses by a set of "components" demarcated by ~, which represent binding sites or modification sites. As shown in Fig. 2A, CaM has four binding sites for Ca^{2+}, two at the C-terminus and two at the N-terminus; thus, the three states for each terminus (~0,~1, or ~2 of components C or N) represent zero bound Ca^{2+}, one bound Ca^{2+}, or two bound Ca^{2+}, respectively. The camkii component is the binding site for a CaMKII subunit. The model in Pepke et al. (19) did not include CaM trapping following autophosphorylation; CaM-trapping was introduced into the model of the holoenzyme as described below.

CaMKII Holoenzyme. We updated the model of CaMKII subunits within a dodecameric holoenzyme from Ordyan et al. (38). This model employed BioNetGen language (BNGL) and the simulation algorithm NFsim, to build the structure of the holoenzyme, simulate the kinetics of interaction of its subunits with Ca^{2+}/CaM, and simulate the subsequent autophosphorylation and dephosphorylation by phosphatase of individual subunits. Parameters and reactions of subunits in this model were based upon those in Pepke et al. (2010), which have been repeatedly vetted for accuracy.

This model did not include CaM-trapping or spatial dynamics and was originally used to examine the potential influence of neurogranin on integration and summation of autophosphorylation following increases in Ca^{2+} concentration.

In the present, updated model, the individual subunits are specified in BNGL as follows: <CaMKII(l, r, c, T286~0~P, pp1~0~1, T306~0~P, cam~la~ha)> (Fig. 4A). Components l, r, and c are sites of interaction within the holoenzyme; l is a binding site at the left side of the subunit, r at the right side of the subunit, and c (center) a site that interacts with a subunit in the opposite six-membered ring (Fig. 4B). The unphosphorylated subunits were added ("instantiated") into the model by specifying irreversible binding at these three sites (Fig. 4) to comprise fully specified CaMKII holoenzymes. In BNGL syntax, a bond between two molecules is represented as a period and the components involved in binding are followed by a ! (pronounced "bang") and a number. For example a bond between the left side of one subunit and the right side of another is represented as CaMKII(l!1, r, c, T286~0, pp1~0, T306~0, cam~la).CaMKII(l, r!1, c, T286~0, pp1~0, T306~0, cam~la). The ! can be followed by any number so long as the two binding components have the same number. "T286" is the threonine autophosphorylation site that confers Ca^{2+}-independence; it is modeled as having two states, either unphosphorylated (~0) or phosphorylated (~P). Pp1 is a binding site for the catalytic subunit of protein phosphatase-1; it can have two states, either unbound (~0) or bound (~1) to PP1. "T306" is the threonine autophosphorylation site that can be phosphorylated after CaM unbinds from the subunit. The T306 site remained unphosphorylated (~0) in the present study. The "cam" component is the binding site for calmodulin; it can have two states, either low affinity (~la), or high affinity (~ha). The ~ha state is the high affinity state that appears when a subunit is autophosphorylated at T286; i.e the "CaM-trapping" state (see reaction rules below).

Reaction rules. Reaction rules are specified in BNGL as discrete transformations. For example, the rule "CaM(C~0,camkii) + ca ↔ CaM(C~1,camkii) k_on1C, k_off1C" encodes reversible binding of one Ca^{2+} to the C-terminus of CaM for CaM not bound to CaMKII with k_{on} = k_on1C and k_{off} = k_off1C. The rate constants for each rule are used to compute the probability that the transformation occurs when the two molecules involved in a bimolecular transformation collide. Unimolecular transformations occur at a future time step obtained by sampling the expected first-order decay time course given by the rate constant. At run time, a random number generator is initialized with a seed number for each individual simulation that specifies a sequence of random numbers that are used to generate the sequence of Brownian motion random-walk trajectories and the probabilities of transformations for the simulation.

As described above, the model of binding among Ca^{2+}, CaM, and CaMKII subunits in the holoenzyme includes rules for binding/unbinding of Ca^{2+} to each of the four sites on CaM when CaM is not bound to CaMKII, binding/unbinding of each state of CaM to a subunit of CaMKII in the holoenzyme, and binding/unbinding of Ca^{2+} to each of the four sites on CaM when CaM is bound to CaMKII. Binding of CaM to CaMKII increases its affinity for Ca^{2+}, as expected from thermodynamic detailed balance. These rules and experimental parameters are taken from the model in Pepke et al. (19).

Rules are included for autophosphorylation of one subunit of CaMKII by another. Autophosphorylation at Thr 286 occurs between adjacent subunits in a holoenzyme when they were both active, either because they both have bound Ca^{2+}/CaM or because the "right-hand" subunit is already autophosphorylated. We modeled the autophosphorylation reaction as proceeding in one direction around a ring, with the "right-hand" subunit acting as the kinase and the "left-hand" subunit acting as substrate. This situation fits the structural analysis of subunit interactions during autophosphorylation

(84). Parameters that govern the probability of autophosphorylation were derived from measurements in Shifman et al. (83). In that study. autophosphorylation rates (turnover numbers) were measured at 30° C with a temperature controlled quench-flow device for CaMKII bound to wild-type CaM4, and bound to mutant CaM's that bind Ca^{2+} only at the N or C termini (83). We generated 64 permutations of the autophosphorylation rules between neighboring CaMx-bound subunits in a holoenzyme (CaMx denotes CaM with all possible numbers of bound Ca^{2+} ions). Pairs of subunits, both of which contain bound CaM4, undergo autophosphorylation of the left subunit at the rate k_pCaM4 (0.96 s^{-1}, Shifman et al., 2006). All other permutations underwent autophosphorylation of the left subunit at the rate k_pCaMpartial (0.1 s^{-1}), which is a coarse-grained approximation of the rates measured by Shifman et al. (83). Eight rules are included in which the right-hand subunit of a pair is autophosphorylated but no longer has bound CaM and the left hand subunit contains bound CaMx. For these rules, when the target subunit is bound to CaM4, the rate of autophosphorylation is k_pCaM4. When the target subunit was bound to CaM with less than 4 Ca^{2+} ions bound, the rate of autophosphorylation is k_pCaMpartial.

CaM-trapping. Meyer and Schulman (23) showed that the initial binding of Ca^{2+}/CaM to a subunit within the CaMKII holoenzyme occurs with moderate affinity (K_D = ~50 nM). However, following autophosphorylation, the inhibitory domain is moved entirely away from the substrate pocket (84), leading to a greater than 1000-fold higher affinity for CaM, referred to as CaM-trapping (see Introduction, 23, 58, 59). We added reactions to the model to simulate CaM-trapping in order to enable comparison of simulations with and without CaM-trapping. A component state termed cam~la was added to CaMKII subunits representing the initial lower affinity CaM-binding site; the component state cam~ha was added representing the higher affinity site present following autophosphorylation of a subunit. The off rates of individual CaMx species from CaMKII for each state were calculated based on

the necessity that $\Delta G = 0$ around a reaction cycle ("detailed balance," e.g. see 19). We set the rate of transition from cam~la to cam~ha following autophosphorylation equal to the rate of dissociation of CaMx from the cam~la site.

The reactions of CaMKII holoenzymes and CaM and the autophosphorylation reactions were implemented within the spine geometry shown in Fig. 3, which was taken from the model of Ca^{2+} flux described above (12). The inclusion of reactions leading to CaM-trapping by autophosphorylated CaMKII subunits enabled comparison of activation and autophosphorylation kinetics in the presence and absence of CaM-trapping. Inclusion of reactions specifying dephosphorylation by PP1 enabled examination of the effects of variations in the amounts of PP1 activity. Finally, the creation of a version of the model specifying that dephosphorylation by PP1 does not occur when CaM is bound to an autophosphorylated subunit enabled comparison of the kinetics of autophosphorylation with and without blocking of dephosphorylation by bound CaM.

Postsynaptic EPSPs and Action Potentials. A single 25 mV postsynaptic EPSP resulting from release of glutamate from one vesicle activating both AMPA and NMDA receptors was simulated in the program NEURON. The 25 mV peak was the average size for hippocampal CA1 pyramidal neurons, calculated by Harnett et al. (85). Because the NEURON model did not contain glutamate receptors, the excitatory postsynaptic potential (EPSP) was simulated by injecting current into the spine head as an alpha function such that a 25 mV peak EPSP was produced. The peak of the EPSP occurred about 3 ms after release and decayed with a τ of ~10 ms. The time course of the EPSP was saved to the data file "post_epsp_spine_voltage.dat" to be used at runtime.

The APs in the soma and the associated back-propagating APs (bAPs) in the dendrites arising from the two-epoch stimulus were simulated in the program NEURON by injecting current into the axon

hillock of pyramidal neuron, model "j4" (86). The voltages experienced at a spine located on a dendritic branch ~100 µm from the soma were recorded, as described in Refs. (87) and (12). The spine was chosen so that the bAP arrived at the spine 10 ms after the presynaptic AP. The current injection was large enough to reliably initiate an AP in the soma and subsequent bAP, as it would if applied to an axon bundle with many synapses ending on the neuron. The ion channels included in the j4 simulation are described more fully in Ref. (12) and in the NEURON ModelDB (https://senselab.med.yale.edu/ ModelDB/ShowModel.cshtml?model=2488). The time course of the bAP arriving at the spine was saved to the data file "post_bAP_spine_voltage.dat."

A python script (vm_dependent_rates_post.py) was written to add together the changes in membrane potential in the spine resulting from EPSPs during simulations for each seed, and from the bAP arriving 10 msecs after the AP in the soma. We assumed that the EPSP and bAP summed together linearly. There was a reliable 10 ms delay between the generation of the presynaptic spike in the soma and the arrival of the postsynaptic bAP at our single spine in simulations for each seed. In contrast, the release of glutamate and the resulting timing of the EPSP were more variable because of the biologically realistic stochastic elements built into the simulation of release (Fig. S1 E. When glutamate was released, it was most often at 10ms before the arrival of the bAP. However, occasionally, for the reasons discussed above, glutamate release and the associated EPSP did not appear causally linked to the bAP. Two such events are shown at ~2.4 and ~6.2 sec in Fig. S1 C and E, which depict results of a single simulation for seed #50. NMDARs open and flux Ca^{2+} into the spine only when they bind glutamate at the same time that the EPSP and bAP depolarize the spine. The coincidence of these events opens the channel and relieves the Mg^{2+} block that prevents movement of Ca^{2+} through the channel (74, 88). The complex kinetics of the transitions that allow Ca^{2+} flux through the NMDARs are explained in detail in Ref. (12).

Data Analysis. The simulations were performed on an HPC cluster at Caltech on 50 nodes each having at least 256 Gbytes of RAM. Monte Carlo simulations in MCell4 (64) rely on generation of random numbers to determine the diffusion trajectories and probabilities of each reaction. Each simulation was initiated with a different seed for the random-number generator. Simulation of 50 seeds for each condition required 7 to 10 days of compute time. Output, consisting of numbers of molecular states across time, were stored as ASCII data files. MCell permits output of a "checkpoint file," that can

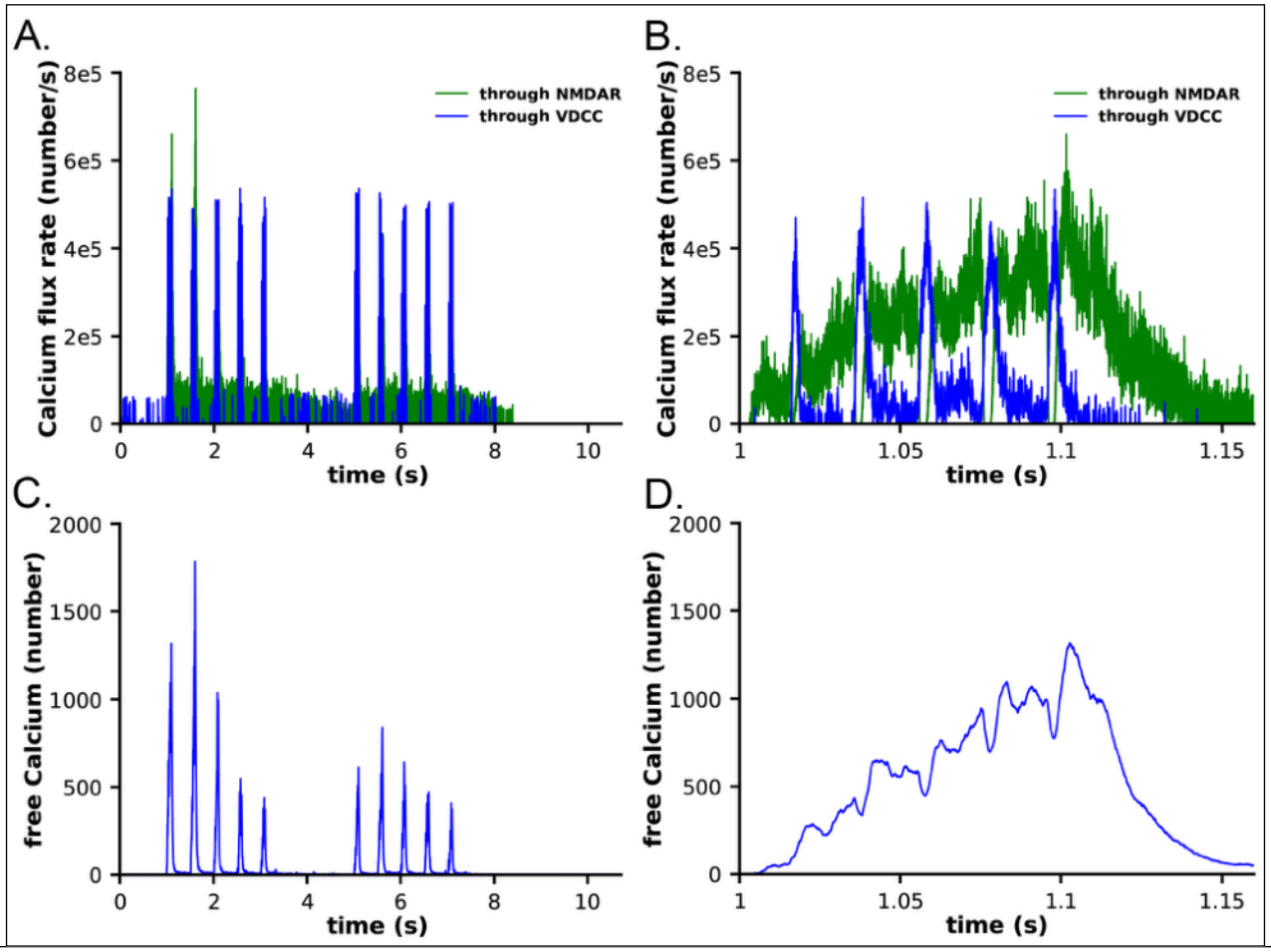

Figure 5: Calcium influx in spines in response to the stimulus shown in Figure 5. **A**. Calcium flux rate through NMDARs (green) and VDCC (blue). **B**. Data from A. between 1 and 1.15 s. **C**. Number of free calcium ions in the spine. **D**. Data from C. between 1 and 1.15 s. Each curve is the average of 50 individual seeds. The dynamics of NMDAR, VDCC, and calcium are the same in the CaM-trapping and non-trapping models. The dynamics of the different CaM species are shown in Fig. S3 A, B.

be used to extend the time of a simulation beyond our standard 11 seconds if desired. The number of individual simulations for each condition required to obtain high confidence averages was determined by comparing the mean and standard deviation of 30, 40, and 50 simulations of calcium dynamics. Our analyses showed that there was no statistically measurable difference between the population averages for 40 and 50 seeds. We thus used 50 seeds for each condition in our simulation to ensure that we would obtain a full representation of all possible stochastic trajectories. All data are plotted as the mean of 50 seeds.

Output was plotted in MatPlotLib (matplotlib.org) or Prism (GraphPad, www.graphpad.com).

The time constant (τ) of exponential decay of pCaMKII caused by dephosphorylation by PP1 was calculated by fitting the amplitude and decay time of averaged curves of pCaMKII with an equation for a single exponential.

Materials Availability. The suppementary movie and the eight models used to generate the data reported here are available for download as a compressed file at: http://www.mcell.cnl.salk.edu/models/spatial-model-of-CaMKII-2024-1/. They are also available on Zenodo at https://doi.org/10.5281/zenodo.12764450. MCell4 is available for download at http://mcell.org/ and as source code at http://github.com/mcellteam/mcell.

Results:

Calcium dynamics in the spine in response to the two-epoch stimulus. We first evaluated Ca^{2+} influx into the spine through the NMDARs and VDCCs in response to the two-epoch stimulus shown in Fig. S1. As in our previous study (12), the model captured the complex and stochastic kinetics of NMDAR and VDCC channel openings (Fig. S2). The NMDAR channel was opened by binding of glutamate, and the Mg^{2+} block of Ca^{2+} flux was relieved by depolarization of the membrane during the

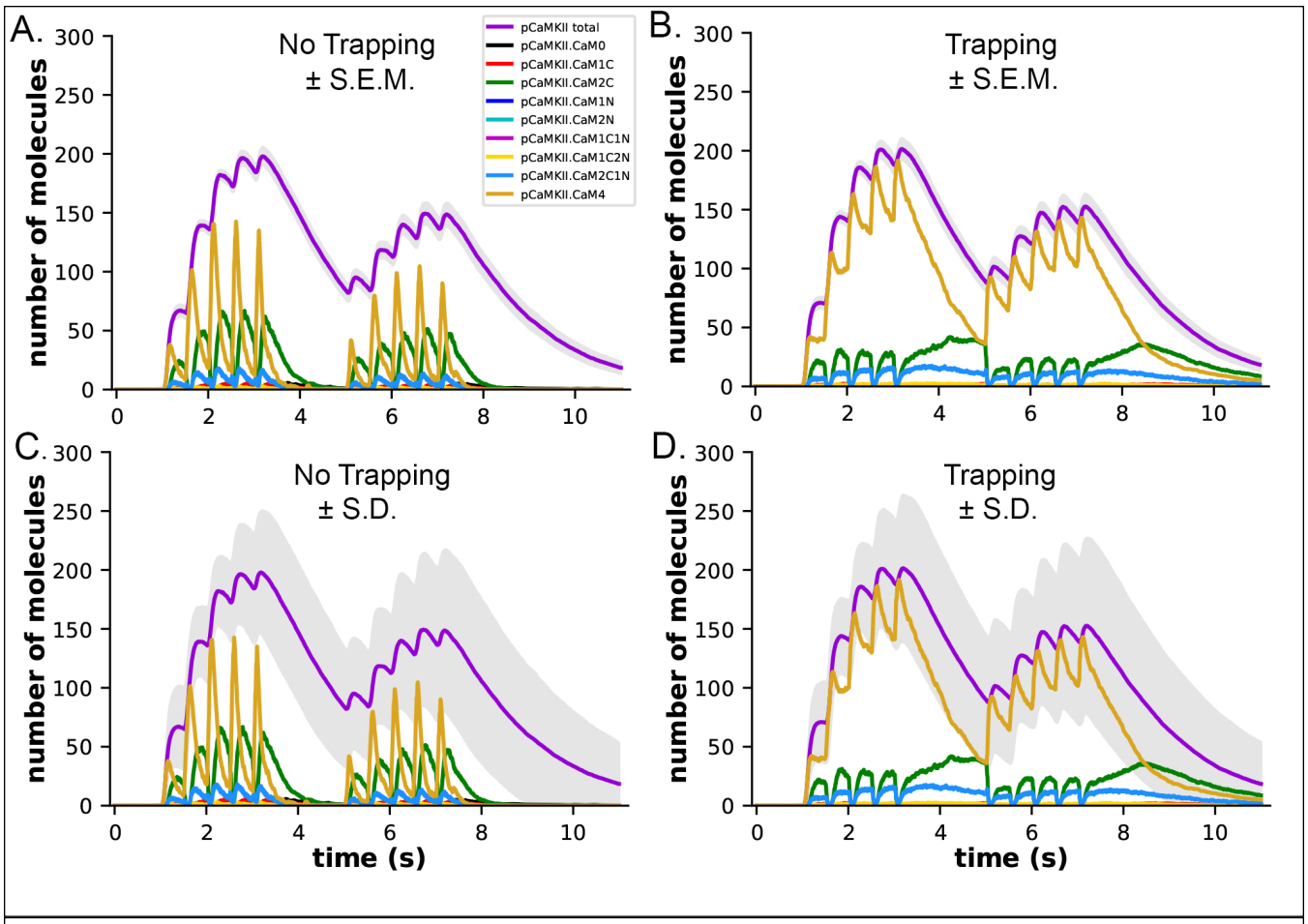

Figure 6: Dynamics of formation of phosphorylated subunits of CaMKII (pCaMKII) and binding of CaM species to them in the presence and absence of CaM-trapping. **A**. Binding of calcium-bound states of CaM to pCaMKII in the absence of CaM-trapping. Colors are as in the legend. **B**. Binding of calcium-bound states of CaM to pCaMKII in the presence of CaM-trapping. Curves are the average of 50 simulations initiated by different seeds. The gray shading surrounding the curve depicting formation of pCaMKII (magenta) indicates +/- s.e.m. **C.** and **D**. The same curves as depicted in A and B, but with the gray shading surrounding the curve depicting formation of pCaMKII indicating +/- s.d. The large standard deviation results from the number of stochastic reactions in the model. The large variation reflects the biological reality of coupled reactions occurring among a limited number of molecules in a small cellular space. See Supplementary Material for a short movie of a simulation with glyphs as shown in Fig. 3 B,C.

bAP (Fig. S2 A,B). During the first epoch, the number of open NMDAR channels decreased for the later

three bursts of APs, reflecting the decrease in the number of vesicles releasing glutamate (Figure S1 C). The bAPs continued to relieve the Mg^{2+} block for all open NMDAR channels (Fig. S2 A, B). The number of open NMDAR channels decreased substantially for the second epoch due to the lower release probability from the presynaptic terminal caused by short term depression (Fig. S1 C) and a small effect of NMDAR desensitization. The stimulus caused voltage-dependent openings of the single VDCC in the spine (Fig. S2 C, D).

The stimulus resulted in calcium influx into the spine through NMDARs and VDCCs (Fig. 5). Fluxes through NMDARs and VDCCs corresponded to the channel opening dynamics shown in Fig. S2. Although the peak Ca^{2+} flux through the VDCC was greater than that through the NMDARs, the integrated flux through NMDARs was considerably greater than the integrated flux through the VDCC, as is evident in Fig. 5B. As a result of these fluxes, the free Ca^{2+} in the spine increased in response to the stimulus (Fig. 5 C, D), as did all of the Ca^{2+}-bound species of free CaM (Figs. S3 and S4). Total free Ca^{2+} entering during the first epoch was greater than that during the second epoch due to synaptic depression. In this model, CaM can diffuse from the shaft into the spine during the stimulus; thus, the total Ca^{2+}-bound CaM and CaM bound to CaMKII exceeded the amount of CaM initially added to the spine alone.

Dependence of the dynamics of CaM binding to CaMKII on CaM-trapping. We measured the dynamics of formation of phosphorylated CaMKII subunits (pCaMKII) in the absence (Fig. 6A) and presence (Fig. 6B) of CaM-trapping. Each phosphorylated CaMKII subunit could be bound to CaM in any one of eight states; CaM with no bound Ca^{2+} (CaM0), or CaM with 1 to 4 bound Ca^{2+}'s (CaM1C, CaM2C, CaM1C1N, CaM2C1N, CaM2N, CaM1C2N, and CaM4). The results show that the total accumulation of pCaMKII was independent of the presence of CaM-trapping with the stimulus applied

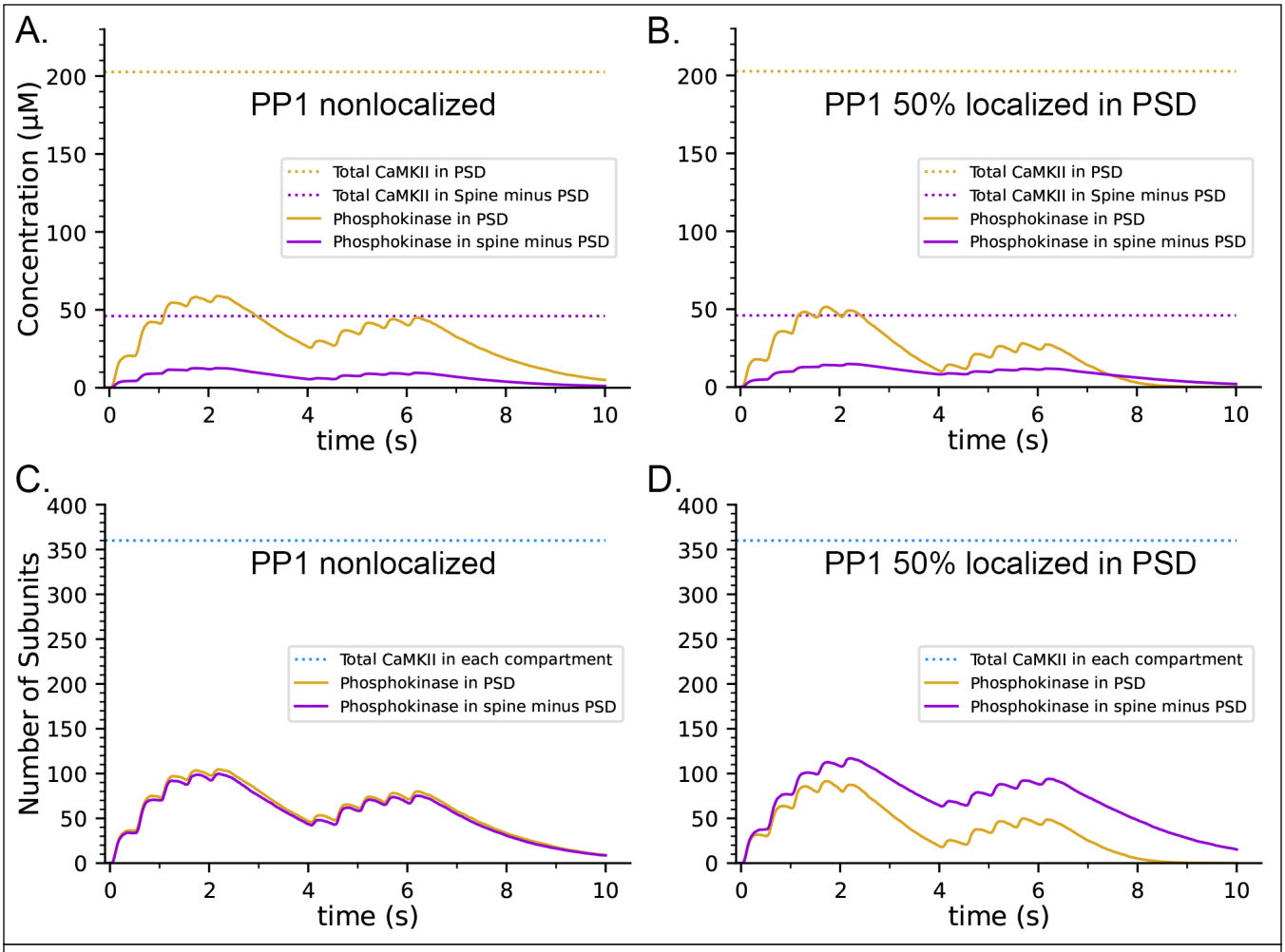

Figure 7. Effects on the dynamics of formation of phosphorylated subunits of CaMKII (pCaMKII) of localization of 50% of CaMKII in the PSD and of 50% of PP1 in the PSD. Lines and colors are as in the legends. **A**. Concentration of pCaMKII in the PSD capsule and in the rest of the spine (minus the PSD capsule) compared to the total CaMKII in each compartment. **B**. Same as in A, but with 50% of PP1 localized in the capsule. **C**. Numbers of pCaMKII in the PSD capsule and in the rest of the spine, compared to the total CaMKII in each compartment. **D**. Same as in C, but with 50% of PP1 localized in the capsule.

here. In the presence or absence of CaM-trapping, the numbers of pCaMKII subunits bound to CaM0, CaM1C, CaM1N, CaM2N, CaM1C1N, and CaM1C2N were negligible. In the presence of CaM-trapping, binding of CaM4, CaM2C, and CaM2C1N to pCaMKII was substantially prolonged, and the numbers of these bound CaM species did not fall to zero before the onset of the second epoch (Fig. 6B, D). However, because these species are bound to CaMKII subunits that are already autophosphorylated,

the prolonged binding did not increase the likelihood that newly bound CaM during the second epoch would be located next to an active subunit. The presence of trapping did not significantly increase the lifetime of CaM species bound to non-phosphorylated subunits (Fig. S5). For this reason, CaM-trapping did not increase the number of autophosphorylated subunits produced by the stimulus.

Figures 6A and B show the small s.e.m. of formation of pCaMKII averaged over 50 seeds (grey shading), indicating the high accuracy of our calculation of the mean pCaMKII. In contrast, the large s.d. of pCaMKII (Fig. 6C, D, grey shading), captures the large dispersion of data that arose because each seed produces a distinct trajectory of binding and autophosphorylation. The dispersion is the result of the many probabilistic steps involved in formation of pCaMKII upon Ca^{2+} entry. This "noisiness" reflects the actual physiological variability expected for activation of CaMKII in a median-sized synapse by the stimulus that we used.

The effect of localization of CaMKII in the PSD on the dynamics of autophosphorylation. The concentration of CaMKII in the spine cytosol is high; however *in vivo*, a substantial portion of spine CaMKII is further localized to the PSD as shown by immunofluorescence and biochemical studies (89-92)**,** where it is concentrated within ~50 nm of the postsynaptic membrane. It has been suggested that this portion of CaMKII may be more highly activated and autophosphorylated than cytosolic CaMKII during synaptic stimuli that activate NMDARs (93). To test this idea, we created a capsule associated with the postsynaptic membrane. The capsule has lateral boundaries contiguous with the reconstructed PSD and extends 50 nm into the cytoplasm from the inner membrane leaflet. The volume of the capsule is 0.002915 fL which is ~ 20% of the spine volume. The walls of the capsule were made reflective to CaMKII and transparent to all other volume molecules. To simulate 50% localization of CaMKII in the PSD, we placed 30 holoenzymes within the PSD capsule (subunit concentration ~200

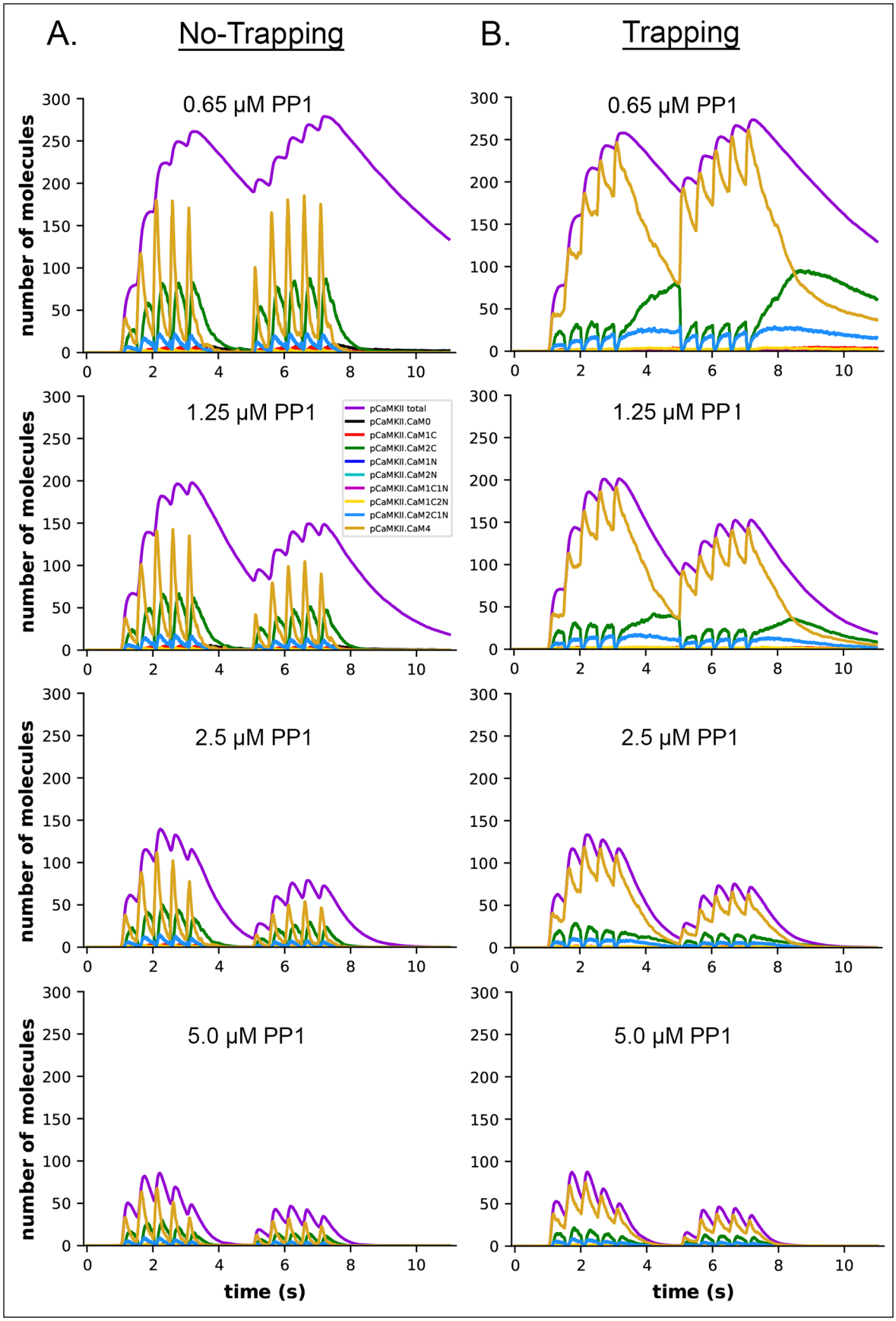
A.
No-Trapping
B.
Trapping
0.65 μM PP1
1.25 μM PP1
2.5 μM PP1
5.0 μM PP1
number of molecules
time (s)
pCaMKII total
pCaMKII.CaM0
pCaMKII.CaM1C
pCaMKII.CaM2C
pCaMKII.CaM1N
pCaMKII.CaM2N
pCaMKII.CaM1C1N
pCaMKII.CaM1C2N
pCaMKII.CaM2C1N
pCaMKII.CaM4

Figure 8: Dynamics of formation of pCaMKII subunits and binding of CaM species to them in the presence of different concentrations of active PP1. **A**. In the absence of CaM-trapping. Concentrations of active PP1 range from 0.65 μM to 5.0 μM, as indicated. **B**. In the presence of CaM-trapping. Concentrations of active PP1 range from 0.65 μM to 5.0 μM, as indicated. Each curve is the average of 50 simulations run with different random seeds.

μM) and 30 holoenzymes in the spine cytosol outside the PSD capsule (subunit concentration ~43 μM)., The other variables in this model were identical to those in the simulations shown in Fig. 6 B and D, which included CaM-trapping. Results of simulations with this model are shown in Fig. 7 A and C. Localization of CaMKII in the PSD has only a minimal effect on the proportion of subunits autophosphorylated (Fig. 7C), indicating a small enhancement of autophosphorylation likely arising from the proximity of subunits in the PSD to Ca^{2+} coming through the NMDA receptor. However, as expected, the concentration of pCaMKII in the PSD is approximately 5-fold higher than in the rest of the spine (Fig. 7A). Note that that the increased concentration of CaMKII in the PSD does not alter the rate of autophosphorylation upon CaM binding because autophosphorylation is an intraholoenzyme reaction. The higher concentration of CaMKII would enhance the rate of binding of pCaMKII to the nearby GluN2B subunits of the NMDARs (26, 94) and to densin-180 located in the PSD (95, 96), and the rate of autophosphorylation of protein substrates located in the PSD.

It has been reported that pCaMKII is preferentially dephosphorylated by PP1 localized in the PSD (53). To test the effect of localization of PP1 in the PSD, we further modified the model to make the capsule reflective to both CaMKII and PP1; and placed 50% of CaMKII and of PP1 (6 molecules, concentration ~3.3 μM) inside the capsule leaving the other 50% in the rest of the spine cytosol (concentration ~0.7 μM). Simulations with this modified model revealed that differential localization of PP1 in the PSD decreased formation of pCaMKII in the PSD and enhanced formation of pCaMKII

outside the PSD (Fig. 7 B and D). It is notable that the numbers and activity of PP1 in our models were not adjusted to confer sensitivity to PP1, rather they were set according to measurements in the experimental literature as described below. Thus, the results are consistent with and reinforce the hypothesis that the sensitivity of induction of LTP to the level of phosphatase activity observed experimentally (62, 97) is a result of the high sensitivity of CaMKII autophosphorylation to PP1 activity in the spine.

The dynamics of autophosphorylation of CaMKII are highly sensitive to the concentration of active phosphatase. The results in Fig. 6 were obtained with a uniform concentration throughout the spine of CaMKII subunits (80 μM subunits) and active PP1 **(**1.25 μM). We chose this amount as a likely median concentration based on the study of Ingebritsen et al. (79)**.** The PP1 catalytic subunit is regulated and localized *in vivo* by a variety of specialized regulatory subunits (98, 99), including in synapses by neurabin (100, 101) and spinophilin (102). Thus, the level of PP1 activity in synaptic spines is likely to be variable and may be regulated by synaptic activity. For this reason, we varied the concentration of active PP1 in the spine during a set of simulations to measure the sensitivity of autophosphorylation to levels of active PP1 during the stimulus. The extent of formation of pCaMKII was extremely sensitive to the level of PP1 (Fig. 8). The number of autophosphorylated subunits (pCaMKII) remaining at 5 min, which was the time of initiation of the second epoch, was more than doubled (from 90 to 192) when the amount of active PP1 was reduced by half from 1.25 μM to 0.65 μM (Fig. 7). The number of active PP1 molecules bound to a CaMKII subunit at the peak of the first epoch was nearly linearly dependent on the concentration of PP1 between 0.65 and 1.25 μM (Fig. S6).

In the lowest concentration of PP1 (0.65 μM), the residual number of pCaMKII remaining after the first epoch (~190 out of a total of 720 subunits or 25%) was sufficient to support an absolute increase in

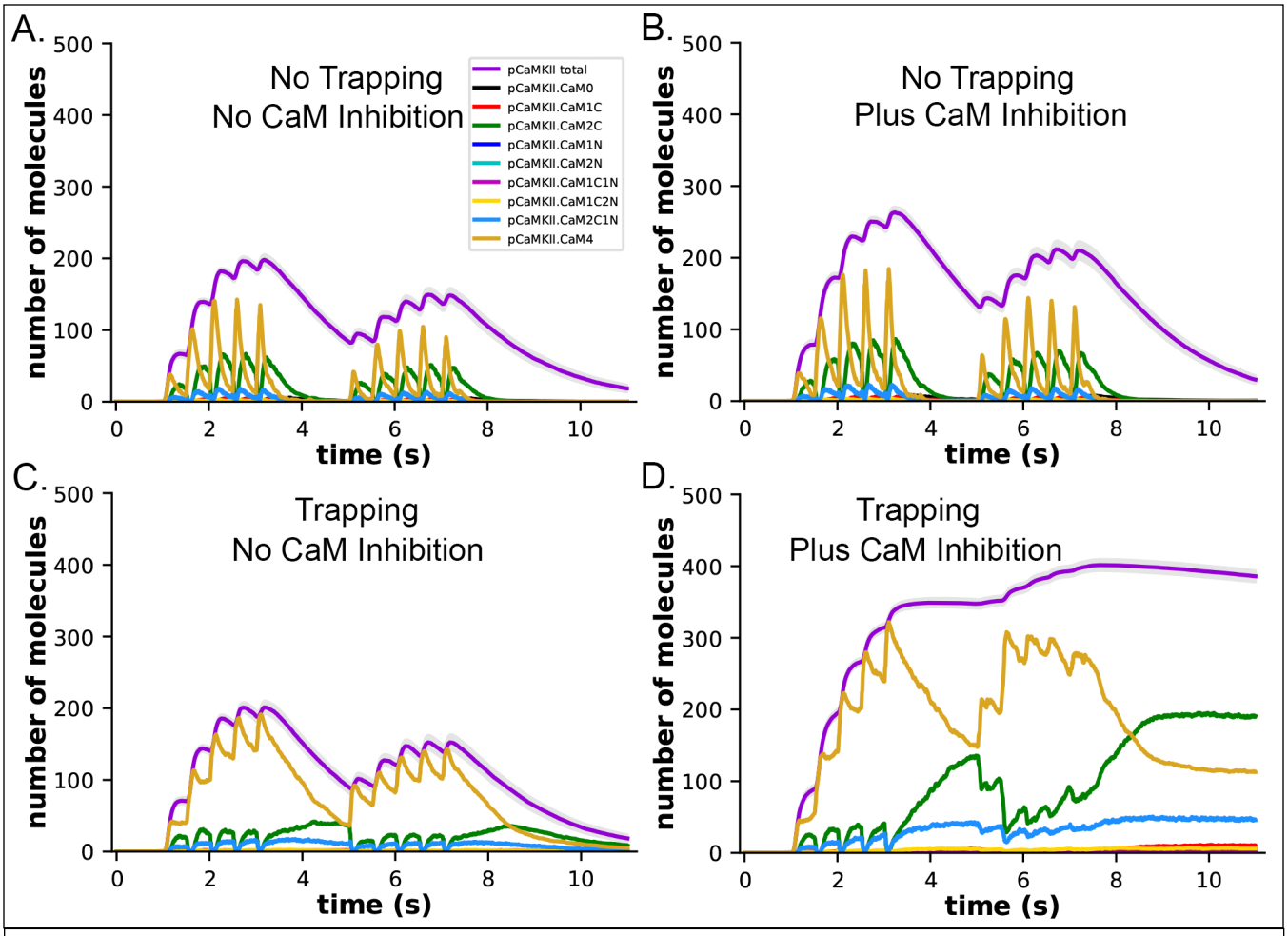

Figure 9. Dynamics of formation of pCaMKII by competition for binding between PP1 and CaM, in the presence and absence of CaM-trapping. **A**. Data replotted from Fig. 5A (no trapping) for comparison to B. **B**. Dynamics of formation of pCaMKII in the presence of competition between CaM and PP1, and in the absence of trapping. **C**. Data replotted from Fig. 5B (trapping) for comparison to D. **D**. Dynamics of formation of pCaMKII in the presence of competition between CaM and PP1, and in the presence of trapping. Each curve is the average of 50 simulations with 1.25 μM PP1, initiated with different random seeds.

pCaMKII during the second epoch despite the reduced influx of Ca^{2+} (see Fig. S2 C). With 25% of subunits autophosphorylated, the average number of pCaMKII subunits in a six-membered ring would be ~1.5. In contrast, In 1.25 μM PP1, the average number of pCaMKII was ~90 out of 720 or ~12.5%, with an average of ~0.75 pCaMKII in a six-membered ring. To become newly autophosphorylated, a subunit with newly bound CaMx needs to be located next to an activated subunit in the clockwise

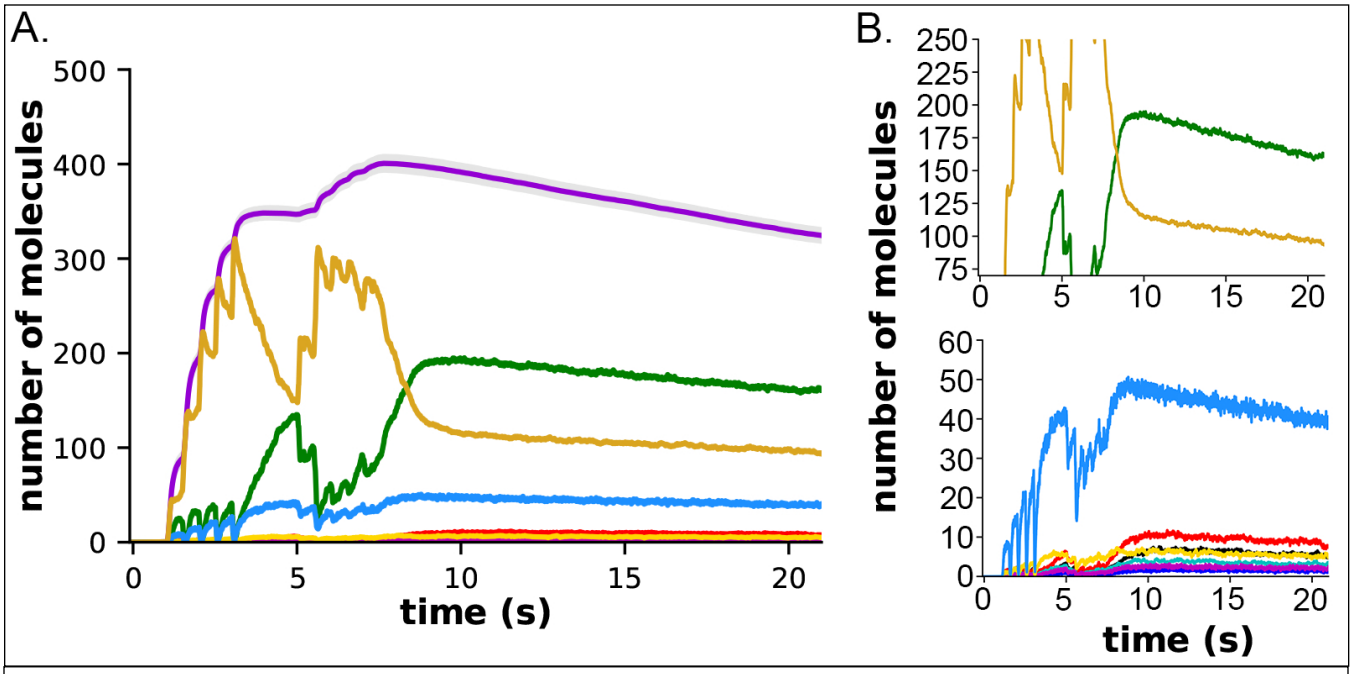

Figure 10. Formation and decay of pCaMKII and bound CaM species after the two-epoch stimulus. **A.** The simulations depicted in Fig. 9D were extended for an additional 10 seconds to measure the rate of dephosphorylation of pCaMKII in the presence of competition for binding between CaM and PP1. **B.** Data from A. plotted with magnified y-axes to show visible decay of bound CaM4, CaM2C (top) and CaM2C1N (bottom). The decay constant for dephosphorylation measured from this data are shown in Table 1.

direction. A decrease in active PP1 from 1.25 μM to 0.65 μM, increases the probability of this occurring from ~0.75/5.25 (14%) to ~1.5/4.5 (33%). This higher probability increases the likelihood that a subunit with newly bound CaMx will be able to be autophosphorylated by its neighbor. The data provide quantitative detail about how the interplay between activation or inhibition of PP1 can exert exquisitely tight control of the progression of activation of CaMKII by a given stimulus.

CaM-trapping may influence the rate of dephosphorylation of pCaMKII by prolonging the ability of bound CaM to inhibit binding of PP1. The presence of CaM-trapping did not influence the rate or extent of formation of pCaMKII during the two epoch stimulus that we used here (Compare Figs. 6 A and B). However, it did significantly prolong the lifetimes of binding of CaM4, CaM2C, and CaM2C1N to CaMKII. In an an earlier modeling study (63), it was noted that the CaM-binding domain

[PP1]	τ Non-trapping		τ Trapping		τ Non-trapping CaM vs. PP1 competition		τ Trapping CaM vs. PP1 competition	
	Epoch 1	Epoch 2	Epoch 1	Epoch 2	Epoch 1	Epoch 2	Epoch 1	Epoch 2
0.65 μM	5.0 s	4.9 s	5.01 s	4.8 s				
1.25 μM	1.9 s	1.7 s	2.0 s	1.8 s	2.3 s	1.9 s	60.4 s	60.4 s
2.5 μM	0.74 s	0.65 s	0.74 s	0.67 s				
5.0 μM	0.33 s	0.32 s	0.38 s	0.32 s				

Table 1. Values of tau for dephosphorylation of pCaMKII in the non-trapping and trapping cases were determined at different simulated concentrations of PP1 from the data shown in Figures 9 and 10, respectively, as described under Methods. The values of tau in the presence of competition for binding between CaM and PP1 were determined for the non-trapping case from the data shown in Fig. 10 B, and for the trapping case from Fig. 11. The tau for Epoch 1 was identical to that of Epoch 2 as determined by measuring the decay of pCaMKII from the peak at 4 secs to 5 secs, which was identical to that of Epoch 2 from the peak at 7.7 secs to 8.7 secs. Tau's for CaM4, CaM2C, and CaM2C1N from Fig. 13B were 61.7, 57.2, and 59.2, respectively.

on CaMKII overlaps significantly with the region on the CaMKII regulatory domain immediately downstream of T286, near where PP1 would bind to catalyze dephosphorylation of T286. Therefore, the authors suggested that bound CaM might block or partially inhibit reversal by PP1 of CaMKII autophosphorylation. The molecular mechanism by which PP1 is targeted to T286 is not known in detail. However, the suggestion that bound CaM might interfere with binding of PP1 is supported by structural studies of binding of the PP1 catalytic subunit to substrates (98) and to the targeting subunit spinophilin (103). PP1 interacts with both classes of proteins over a wide area of its surface. This property of PP1, together with the large size of the spinophilin targeting subunit (104), suggests that bound CaM would sterically hinder binding of PP1 to CaMKII in the vicinity of phosphorylated T286, and thus inhibit dephosphorylation.

To measure the effect of CaM-trapping on the postulated inhibition of PP1 dephosphorylation by bound CaM, we modified the reaction rules for dephosphorylation to allow PP1 to bind to a pCaMKII subunit only when the cam site is free. This situation represents the most extreme case in which bound CaM completely blocks PP1 binding. Because a PP1 holoenzyme likely binds to pCaMKII via more than one docking site (98), it is also possible that bound CaM lowers the affinity for PP1 by steric hindrance, but does not block dephosphorylation completely. We did not investigate this latter possibility in the present study.

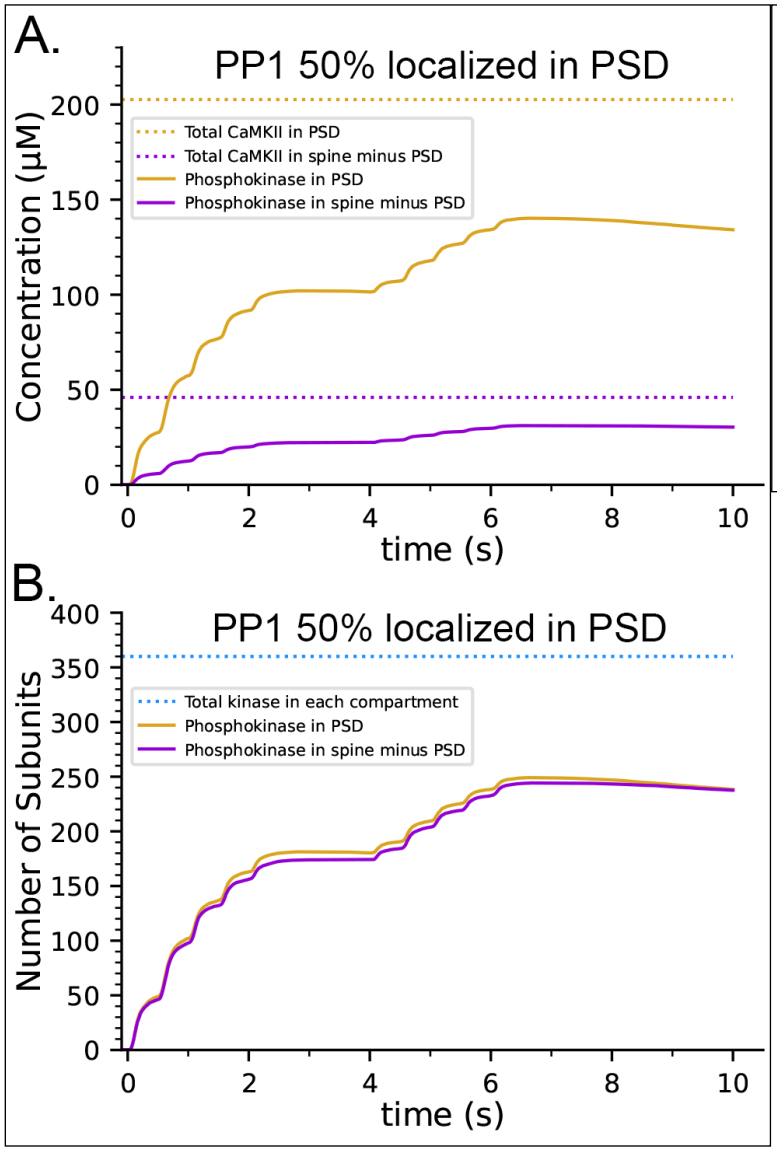

Figure 11. Effect of inhibition of PP1 activity by bound CaM on autophosphorylation when both CaMKII and PP1 are differentially localized in the PSD. **A**. The concentration of pCaMKII reaches ~67% of the possible maximum of ~200 μm in the PSD. **B**. The proportion of autophosphorylated subunits in a holoenzyme is ~67% in both compartments.

In both the presence and absence of CaM-trapping, the inclusion of inhibition by CaM of PP1 binding to CaMKII increased the maximum formation of pCaMKII (Compare Fig. 9 A,C to B, D). However, the combined effect of inhibition by CaM and CaM-trapping was profound, increasing the rate-constant τ for dephosphorylation from ~1.8

s to 60.4 s (Table 1) and resulting in autophosphorylation of approximately half of the CaMKII subunits at peak during the second epoch (Fig. 9D, Fig. 10). Thus, the model predicts that the rate of decay of pCaMKII after a stimulus is intricately coupled to the relative affinities of binding among CaM, PP1, and CaMKII.

To evaluate the effect of inhibition by CaM when both CaMKII and PP1 are 50% localized in the PSD capsule, we added the inhibition rules to the localization model shown in Fig. 7. In simulations of this model, the maximum concentration of pCaMKII formed in the PSD during the stimulus increased almost 3-fold from about ~50 μM (Fig. 7 B) to ~140 μM (Fig. 11 A). Although ~67% of subunits were autophosphorylated at the peak, the concentration of pCaMKII continued to decay slowly when the stimulus ended (Fig. 11 A, B). When 50% of CaMKII and PP1 were both sequestered in the PSD capsule (Fig. 11), the rate of decay (τ) in the capsule was 54.5 s and the rate in the cytosol outside the capsule was 72.0 s, compared to 60.4 s when neither are sequestered (Table 1). These results mean that, under these physiological conditions, dephosphorylation by PP1 is not overwhelmed by the rate of recurring autophosphorylation within the holoenzyme, even when maximum autophosphorylation reaches 67% of the total subunits.

Discussion:

We developed a series of agent-based stochastic computational models to examine the responses of CaMKII holoenzymes during the first 20 secs after a two-epoch stimulus of medium strength in a median-sized spine. The models are based upon three earlier carefully-vetted published models (12, 19, 38). They contain physiologically realistic numbers of proteins situated in a spine from hippocampal neuropil (12). The numbers and kinetic parameters of the added CaMKII holoenzymes, CaM, and PP1

are drawn from measurements made over several years during biochemical and electrophysiological experiments cited in the text. Parameters are adjusted to 30-35° C.

The use of experimentally measured parameters and realistic numbers and spatial arrangements of the relevant proteins enabled us to test several hypotheses about the behavior of CaMKII under conditions present *in vivo*.

We tested the hypothesis that CaM-trapping may result in an enhanced, non-linear increase in autophosphorylation of CaMKII during high frequency synaptic stimulation (De Koninck and Schulman, 1998; Nicoll and Schulman, 2023; Putney, 1998). We found that, while CaM-trapping does indeed prolong the association of CaM with autophosphorylated CaMKII subunits, it does not alter the extent of autophosphorylation during the repeated stimuli in the 50 Hz frequency range that we used here. This is because the association of CaM with non-autophosphorylated subunits is not prolonged by trapping, and, thus, the probability of autophosphorylation is not increased during the second epoch.

We found that the total amount of autophosphorylation of CaMKII during the two-epoch stimulus is highly sensitive to small changes in the level of active PP1 within the physiological range of 0.65 to 5.0 μM (e.g. Ingebritsen et al., 1983, Figs 10, 12). This finding is consistent with previous experimental evidence for a role of PP1 in regulation of synaptic plasticity. PP1 is specifically enriched in synaptic spines (53, 105), and has been shown in several studies to regulate the direction and magnitude of changes in synaptic strength produced by different frequencies of stimulation. Under baseline conditions in slices from hippocampal area CA1, low frequency stimulation (1-3 Hz) leads to induction of long-term depression (LTD); stimulation at ~10 Hz is "neutral," producing no change in synaptic strength, and higher frequency stimulation in the range of 25 -100 Hz induces long-term potentiation (LTP) (97, 106). However, this relationship between stimulus intensity and the direction of change in synaptic

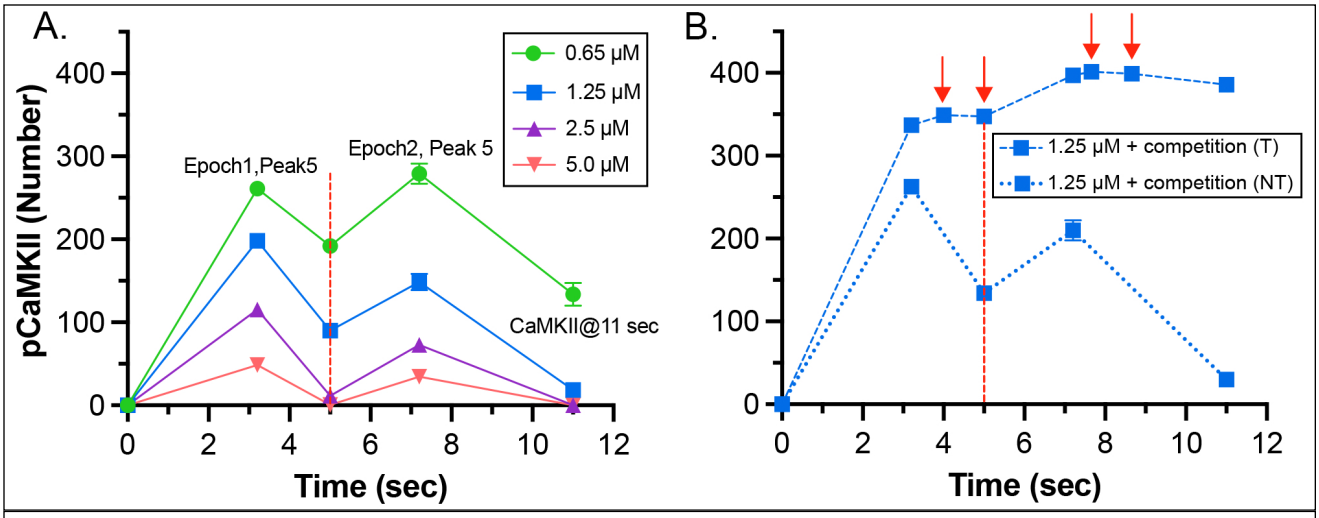

Figure 12. A. Peak concentrations of pCaMKII during the two epoch stimulus in the presence of increasing concentrations of active PP1. Data are replotted for comparison from the results shown in Fig. 8. The dotted red line at 5 sec marks the time of initiation of the second epoch of the stimulus. Average5/50s ± s.e.m. of 50 simulations. **B**. Peak concentrations of pCaMKII during the two epoch stimulus including competition between binding of CaMx and PP1. Data with (T) and without CaM-trapping (NT) are replotted from the results shown in Fig. 9D. In the graph of the model that includes CaM-trapping, points at 4 and 5 sec and at 7.7 and 8.7 secs are marked with red arrows. The differences in numbers of pCaMKII at these times were used to compare the decay time after the first and second epochs. S.e.m.'s for most of the measurements are smaller than the symbols.

strength is altered by pharmacological agents that inhibit PP1 phosphatase activity (97, 107). For example, induction of LTD by stimulation at 1 Hz is blocked by application of inhibitors of PP1 (108). Conversely, induction of LTP is potentiated by inhibition of PP1 (109). Cyclic AMP-regulated inhibition of PP1 acts as a "gate" that determines whether LTP is produced by a given stimulus. For example, activation of the cAMP pathway by a variety of pharmacological agents permits induction of LTP by both widely spaced "HFS" stimulation (3 pulses of 900 APs at 100 Hz separated by 10 min, 62) and by "θ pulse" stimulation in the 5-12 Hz range (97). When the increase in cAMP is blocked, these stimuli do not induce LTP. Activation of β-adrenergic receptors by noradrenaline also increases LTP at

hippocampal synapses through the cAMP pathway that inhibits PP1, suggesting that this mechanism is responsible for the enhancement of learning by noradrenaline (110). Notably, we did not adjust the concentration of PP1, or its parameters, in this model to achieve a particular outcome in the simulations. Rather, we chose what we considered to be the best estimates of these parameters from the biochemical literature. Thus, the agreement between experimental findings showing sensitivity of synaptic plasticity to PP1 activity and the sensitivity of autophosphorylation to PP1 activity in our simulations, shows that, as a first approximation, our model reproduces behavior that would be expected *in vivo*.

A third, and unanticipated, finding is that one function of CaM-trapping may be to dramatically alter the sensitivity of autophosphorylation to PP1 activity. This finding is based on the structural prediction that binding of CaM to an autophosphorylated subunit of CaMKII is likely to sterically hinder binding of PP1 required for dephosphorylation of T286 (63). The PP1 catalytic subunit interacts with substrates over an unusually large surface area comprising three different surface domains that surround the active site (98). The recognition pockets for PP1 on substrates are usually more distant from the phosphorylated residue than the typical consensus recognition sequences for protein kinases (104). Binding of PP1 to a substrate via two or more of its surface domains provides avidity that increases the K_M and thus, the rate of dephosphorylation. Conversely, reducing interaction of a substrate with one of the surface domains reduces the K_M and slows the rate of dephosphorylation. The targeting of PP1 to subcellular domains, and its substrate specificity, are regulated by association with a wide array of different subunits to form multi-subunit holoenzymes (98, 104). In dendritic spines, the predominant targeting subunit for PP1 is spinophilin (111, 112), which binds to spine actin filaments (113). The spinophilin-PP1 holoenzyme, with a molecular mass of ~150 kDal, is much larger than a CaMKII subunit. Bound spinophilin obstructs one of the three substrate-binding patches on the surface of the PP1

catalytic subunit (103). Thus, the spinophilin-PP1 holoenzyme would be expected to associate with substrates, including CaMKII, via the two remaining binding patches on the catalytic subunit (98). The precise recognition sites for PP1 on CaMKII have not been identified. However, CaM binds to CaMKII at a site located ~ 7 residues downstream of T286 (Fig. 2). Therefore, it is likely to partially, or fully, sterically hinder access of PP1 to phosphorylated T286.

To investigate the effect of competition between CaM-binding and dephosphorylation by PP1, we simulated the most extreme possibility which is complete block of dephosphorylation of T286 by bound CaM. In the absence of CaM-trapping, full blocking of PP1 by bound CaM increased the τ for dephosphorylation by ~10-20% (Table 1). In contrast, when CaM-trapping was included in the model, dephosphorylation was dramatically slowed (Fig. 12). The τ for dephosphorylation was increased 30-fold to 60.2 sec, reflecting the much longer k_{off} for trapped CaM. The number of autophosphorylated subunits per CaMKII holoenzyme at the peak of the two-epoch 50 Hz stimulus doubled from ~200 pCaMKII subunits to ~400, out of the total of 720 subunits. Even this extreme competitive effect would prolong the lifetimes of autophosphorylated subunits for only a few minutes after the Ca^{2+} concentration returns to baseline. The actual effect of CaM-trapping *in vivo* on the rate of dephosphorylation of T286 by PP1 may be less than 100%.

Competition between CaM-binding to pCaMKII and dephosphorylation of T286 by PP1 has not been adequately investigated experimentally. The only experimental study we are aware of that indirectly addressed the competition is Bradshaw et al. (80). These authors sought to provide evidence for a bistable kinase switch comprised of CaMKII and PP1. Their experiments indicated that bound CaM did not interfere with dephosphorylation of Thr286 by PP1. However, the experiments were carried out at 0° C to suppress autophosphorylation of Thr305/306; in addition, they used a ratio of PP1 to

CaMKII that was considerably higher than would be predicted *in vivo* from the measured concentrations that we used in our simulations. In Bradshaw et al., the ratio of PP1 to CaMKII subunits was ~1 to 10 compared to ~1 to 80 in our simulations. Thus, it is possible that in the Bradshaw study, inhibition of PP1 activity by bound CaM was not evident due to the assay conditions.

Many computational models of activation of CaMKII, incorporating various levels of detail and complexity, have been created previously. One conceptually attractive idea has been particularly persistent in these studies — the notion that CaMKII may act as a bistable switch that shifts between an active highly autophosphorylated stable steady-state reflecting LTP and an inactive non-autophosphorylated stable steady-state reflecting LTD (35, 93, 114-118). Because the notion of bistability focuses on steady state behavior, it has been encoded in deterministic equations that specify multiple steady states (116). These models usually include a control parameter that can change the steady state from the low stable state to the high stable state and have been used in mathematical biology to hypothesize that this behavior can occur in complex biological systems (For an introduction, see 119.). As a result, the notion of bistability of CaMKII activity, while appealing in its simplicity, did not evolve from the measured biochemical interactions of CaMKII, CaM, protein phosphatases, or other proposed key proteins. The models detailed here account for the measured rates of autophosphorylation of subunits within a holoenzyme and incorporate measured parameters for the detailed biochemical interactions among CaMKII, CaM, and PP1 (19, 38). With these models, and other previous models that incorporate more biochemical detail (63, 120), bistability of CaMKII is not observed.

We find that, while CaM-trapping alone does not increase the decay time of pCaMKII, the presence of both CaM-trapping and inhibition by CaM of PP1 binding can lead to a prolonged, but not permanent, 'high' level of pCaMKII, perhaps lasting several minutes. This finding suggests that another

form of kinetic regulation may be operating that is sometimes referred to as “kinetic proof-reading” (121, 122). This mechanism involves a biochemical network that is structures in such a way that a series of reversible biochemical steps lead to an essentially irreversible one. The irreversible step only occurs when the preceding reversible steps (i.e. binding between two molecules) last long enough to trigger the next step. The canonical example of kinetic proof-reading is the selection of the correct amino acid-tRNA complex to match a codon on ribosomal bound mRNA during protein synthesis. Only an exact match between the tRNA and mRNA codons results in binding that lasts long enough for irreversible formation of the peptide bond to occur (121).

We propose that to induce LTP, autophosphorylation of CaMKII subunits does not need to reach a the high, irreversible steady-state postulated by the bistable switch theory (e.g. 115, 123). Rather, the convergence of signals at the synapse must simply result in a transient high level of autophosphorylation that lasts long enough to trigger one or more downstream, essentially irreversible, steps causing potentiation of the synapse. One such ‘irreversible’ step might include binding of a critical number of active CaMKII subunits to the carboxyl tails of GluN2B subunits of NMDA-receptors (27, 94, 124). Another might be sufficient dissolution of the protein condensate between PSD-95 and synGAP to trigger irreversible remodeling of the PSD by addition of AMPARs and enlargement of the supporting actin cytoskeleton (5, 29, 40, 125). Both of these events have been proposed to be critical for development and maintenance of LTP.

Several distinct signals can converge on a synapse to modulate the extent of autophosphorylation of CaMKII. The primary signal observed experimentally is repeated high frequency (50-100 Hz) synaptic activation that causes firing of the neuron (see 9, 17). In addition, activation of the cAMP pathway can inhibit PP1, prolonging the lifetime of autophosphorylated CaMKII (32, 62, 97, 110, 126). Src and Fyn

protein kinases, activated by G-protein-coupled receptors, receptor tyrosine kinases, and/or cytokines increase the flux of Ca^{2+} through NMDARs, potentiating induction of LTP by high frequency stimulation (127). Kinetic proof-reading would allow combinations of these signals that lead to sufficiently prolonged autophosphorylation of CaMKII in a synapse to induce LTP.

The model presented here can be expanded to investigate the effects of additional proteins and spatial constraints on regulation of CaMKII and the downstream effects of autophosphorylation. Future investigations will include responses of CaMKII in spines of different sizes, the quantitative effect on autophosphorylation of more prolonged and/or lower and higher frequency stimuli. Importantly, we will investigate the effects of proteins that localize CaM and compete for binding of CaM, and of proteins that regulate PP1. MCell4 is designed to allow introduction of each of these elements in a stepwise fashion to permit dissection of the effects of each and ultimately an understanding of their combined effects.

Acknowledgments:

We acknowledge Prof. T. J. Sejnowski for funding support for T.M.B and M.O, the Air Force Office of Scientific Research (AFOSR) Multidisciplinary University Research Initiative (MURI) grant FA9550-18-1-0051 to P.R., NIH grants MH115456 to M.B.K., DA030749 and MH129066 (CR-CNS) to T.J.S. and M.B.K., and NSF NeuroNex DBI-1707356, NSF NeuroNex DBI-2014862, and NIH MMBioS P41-GM103712 to T.J.S and T.M.B.

Bibliography

1. Magee JC, Johnston D. A synaptically controlled, associative signal for Hebbian plasticity in hippocampal neurons. Science. 1997;275:209-13.
2. Markram H, Lübke J, Frotscher M, Sakmann B. Regulation of synaptic efficacy by coincidence of postsynaptic APs and EPSPs. Science. 1997;275:213-5.
3. Bi G, Poo M-M. Synaptic modifications in cultured hippocampal neurons: dependence on spike timing, synaptic strength, and postsynaptic cell type. J Neurosci. 1998;18:10464-72.
4. Kennedy MB, Beale HC, Carlisle HJ, Washburn LR. Integration of biochemical signalling in spines. Nat Rev Neurosci. 2005;6(6):423-34.
5. Opazo P, Choquet D. A three-step model for the synaptic recruitment of AMPA receptors. Mol Cell Neurosci. 2011;46(1):1-8.
6. Kennedy MB. Synaptic signaling in learning and memory. Cold Spring Harb Perspect Biol. 2013;8:a016824.
7. Biederer T, Kaeser PS, Blanpied TA. Transcellular Nanoalignment of Synaptic Function. Neuron. 2017;96(3):680-96.
8. Bliss TVP, Collingridge GL. A synaptic model of memory: long-term potentiation in the hippocampus. Nature. 1993;361:31-9.
9. Nicoll RA, Schulman H. Synaptic memory and CaMKII. Physiol Rev. 2023;103(4):2877-925.
10. Harris KM, Weinberg RJ. Ultrastructure of synapses in the mammalian brain. Cold Spring Harb Perspect Biol. 2012;4(5).

11. Bartol TM, Bromer C, Kinney J, Chirillo MA, Bourne JN, Harris KM, et al. Nanoconnectomic upper bound on the variability of synaptic plasticity. Elife. 2015;4:e10778.
12. Bartol TM, Keller DX, Kinney JP, Bajaj CL, Harris KM, Sejnowski TJ, et al. Computational reconstitution of spine calcium transients from individual proteins. Front Synaptic Neurosci. 2015;7:article 17.
13. Kennedy MB. Signal-processing machines at the postsynaptic density. Science. 2000;290(5492):750-4.
14. Bourne J, Harris KM. Do thin spines learn to be mushroom spines that remember? Curr Opin Neurobiol. 2007;17(3):381-6.
15. Malenka RC, Bear MF. LTP and LTD: an embarrassment of riches. Neuron. 2004;44(1):5-21.
16. Rosenberg OS, Deindl S, Sung RJ, Nairn AC, Kuriyan J. Structure of the autoinhibited kinase domain of CaMKII and SAXS analysis of the holoenzyme. Cell. 2005;123(5):849-60.
17. Sjostrom PJ, Nelson SB. Spike timing, calcium signals and synaptic plasticity. Curr Opin Neurobiol. 2002;12(3):305-14.
18. Jedrzejewska-Szmek J, Dorman DB, Blackwell KT. Making time and space for calcium control of neuron activity. Curr Opin Neurobiol. 2023;83:102804.
19. Pepke S, Kinzer-Ursem T, Mihalas S, Kennedy MB. A dynamic model of interactions of Ca^{2+}, calmodulin, and catalytic subunits of Ca^{2+}/calmodulin-dependent protein kinase II. PLoS Comput Biol. 2010;6(2):e1000675.
20. Silva AJ, Paylor R, Wehner JM, Tonegawa S. Impaired spatial learning in α-calcium-calmodulin kinase II mutant mice. Science. 1992;257:206-11.

21. Giese KP, Fedorov NB, Filipkowski RK, Silva AJ. Autophosphorylation at Thr286 of the alpha calcium-calmodulin kinase II in LTP and learning. Science. 1998;279(5352):870-3.

22. Miller SG, Kennedy MB. Regulation of brain type II Ca^{2+}/calmodulin-dependent protein kinase by autophosphorylation: a Ca^{2+}-triggered molecular switch. Cell. 1986;44(6):861-70.

23. Meyer T, Hanson PI, Stryer L, Schulman H. Calmodulin trapping by calcium-calmodulin dependent protein kinase. Science. 1992;256(5060):1199-202.

24. Hell JW. CaMKII: claiming center stage in postsynaptic function and organization. Neuron. 2014;81(2):249-65.

25. Bayer KU, Schulman H. CaM Kinase: Still Inspiring at 40. Neuron. 2019;103(3):380-94.

26. Tullis JE, Larsen ME, Rumian NL, Freund RK, Boxer EE, Brown CN, et al. LTP induction by structural rather than enzymatic functions of CaMKII. Nature. 2023;621(7977):146-53.

27. Chen X, Cai Q, Zhou J, Pleasure SJ, Schulman H, Zhang M, et al. CaMKII autophosphorylation is the only enzymatic event required for synaptic memory. Proc Natl Acad Sci U S A. 2024;121(26):e2402783121.

28. Oh JS, Manzerra P, Kennedy MB. Regulation of the neuron-specific Ras GTPase-activating protein, synGAP, by Ca2+/calmodulin-dependent protein kinase II. J Biol Chem. 2004;279(17):17980-8.

29. Araki Y, Zeng M, Zhang M, Huganir RL. Rapid dispersion of SynGAP from synaptic spines triggers AMPA receptor insertion and spine enlargement during LTP. Neuron. 2015;85(1):173-89.

30. Walkup WGt, Washburn L, Sweredoski MJ, Carlisle HJ, Graham RL, Hess S, et al. Phosphorylation of synaptic GTPase-activating protein (synGAP) by Ca^{2+}/calmodulin-dependent protein kinase II (CaMKII) and cyclin-dependent kinase 5 (CDK5) alters the ratio of its GAP activity toward ras and rap GTPases. J Biol Chem. 2015;290(8):4908-27.

31. Diering GH, Huganir RL. The AMPA Receptor Code of Synaptic Plasticity. Neuron. 2018;100(2):314-29.

32. Blitzer RD, Iyengar R, Landau EM. Postsynaptic signaling networks: cellular cogwheels underlying long-term plasticity. Biol Psychiatry. 2005;57(2):113-9.

33. Holmes WR. Models of calmodulin trapping and CaM kinase II activation in a dendritic spine. J Computational Neurosci. 2000;8:65-85.

34. Bhalla US. Biochemical signaling networks decode temporal patterns of synaptic input. J Comput Neurosci. 2002;13(1):49-62.

35. Miller P, Zhabotinsky AM, Lisman JE, Wang XJ. The stability of a stochastic CaMKII switch: dependence on the number of enzyme molecules and protein turnover. PLoS Biol. 2005;3(4):e107.

36. Lisman JE. A mechanism for memory storage insensitive to molecular turnover: a bistable autophosphorylating kinase. Proc Natl Acad Sci U S A. 1985;82(9):3055-7.

37. Nadkarni S, Bartol TM, Sejnowski TJ, Levine H. Modelling vesicular release at hippocampal synapses. PLoS Comput Biol [Internet]. 2010 PMC2978677]; 6(11):[e1000983 p.]. Available from: http://www.ncbi.nlm.nih.gov/pubmed/21085682.

38. Ordyan M, Bartol T, Kennedy M, Rangamani P, Sejnowski T. Interactions between calmodulin and neurogranin govern the dynamics of CaMKII as a leaky integrator. PLoS Comput Biol. 2020;16(7):e1008015.

39. Gaertner TR, Putkey JA, Waxham MN. RC3/Neurogranin and Ca2+/calmodulin-dependent protein kinase II produce opposing effects on the affinity of calmodulin for calcium. J Biol Chem. 2004;279(38):39374-82.

40. Walkup WG, Mastro TL, Schenker LT, Vielmetter J, Hu R, Iancu A, et al. A model for regulation by SynGAP-alpha1 of binding of synaptic proteins to PDZ-domain 'Slots' in the postsynaptic density. Elife. 2016;5:e16813.

41. Araki Y, Rajkovich KE, Gerber EE, Gamache TR, Johnson RC, Tran THN, et al. SynGAP regulates synaptic plasticity and cognition independently of its catalytic activity. Science. 2024;383(6686):eadk1291.

42. Selkoe DJ. Alzheimer's disease. Cold Spring Harb Perspect Biol. 2011;3(7).

43. Mullins C, Fishell G, Tsien RW. Unifying Views of Autism Spectrum Disorders: A Consideration of Autoregulatory Feedback Loops. Neuron. 2016;89(6):1131-56.

44. Scolnick EM. The Path to New Therapies for Schizophrenia and Bipolar Illness. FASEB J. 2017;31(4):1254-9.

45. Bennett MK, Erondu NE, Kennedy MB. Purification and characterization of a calmodulin-dependent protein kinase that is highly concentrated in brain. J Biol Chem. 1983;258:12735-44.

46. Chao LH, Stratton MM, Lee IH, Rosenberg OS, Levitz J, Mandell DJ, et al. A mechanism for tunable autoinhibition in the structure of a human Ca^{2+}/calmodulin- dependent kinase II holoenzyme. Cell. 2011;146(5):732-45.

47. Colbran RJ, Smith MK, Schworer CM, Fong YL, Soderling TR. Regulatory domain of calcium/ calmodulin-dependent protein kinase II. Mechanism of inhibition and regulation by phosphorylation. J Biol Chem. 1989;264(9):4800-4.

48. Miller SG, Patton BL, Kennedy MB. Sequences of autophosphorylation sites in neuronal type II CaM kinase that control Ca^{2+}-independent activity. Neuron. 1988;1:593-604.

49. Schworer CM, Colbran RJ, Keefer JR, Soderling TR. Ca2+/calmodulin-dependent protein kinase II. Identification of a regulatory autophosphorylation site adjacent to the inhibitory and calmodulin-binding domains. J Biol Chem. 1988;263:13486-9.

50. Thiel G, Czernik AJ, Gorelick F, Nairn AC, Greengard P. Ca^{2+}/calmodulin-dependent protein kinase II: identification of threonine-286 as the autophosphorylation site in theasubunit associated with the generation of Ca^{2+}-independent activity. Proc Natl Acad Sci USA. 1988;85:6337-41.

51. Hanson PI, Meyer T, Stryer L, Schulman H. Dual role of calmodulin in autophosphorylation of multifunctional CaM kinase may underlie decoding of calcium signals. Neuron. 1994;12(5):943-56.

52. Shields SM, Ingebritsen TS, Kelly PT. Identification of protein phosphatase 1 in synaptic junctions: dephosphorylation of endogenous calmodulin-dependent kinase II and synapse-enriched phosphoproteins. J Neurosci. 1985;5(12):3414-22.

53. Strack S, Barban MA, Wadzinski BE, Colbran RJ. Differential inactivation of postsynaptic density-associated and soluble Ca2+/calmodulin-dependent protein kinase II by protein phosphatases 1 and 2A. J Neurochem. 1997;68(5):2119-28.

54. Watanabe T, Huang HB, Horiuchi A, da Cruze Silva EF, Hsieh-Wilson L, Allen PB, et al. Protein phosphatase 1 regulation by inhibitors and targeting subunits. Proc Natl Acad Sci U S A. 2001;98(6):3080-5.

55. Monroe JD, Heathcote RD. Protein phosphatases regulate the growth of developing neurites. Int J Dev Neurosci. 2013;31(4):250-7.

56. Platholi J, Hemmings HC, Jr. Modulation of dendritic spines by protein phosphatase-1. Adv Pharmacol. 2021;90:117-44.

57. Sandal P, Jong CJ, Merrill RA, Song J, Strack S. Protein phosphatase 2A - structure, function and role in neurodevelopmental disorders. J Cell Sci. 2021;134(13).

58. Putkey JA, Waxham MN. A peptide model for calmodulin trapping by calcium/calmodulin-dependent protein kinase II. J Biol Chem. 1996;271(47):29619-23.

59. Tse JK, Giannetti AM, Bradshaw JM. Thermodynamics of calmodulin trapping by Ca2+/ calmodulin-dependent protein kinase II: subpicomolar Kd determined using competition titration calorimetry. Biochemistry. 2007;46(13):4017-27.

60. De Koninck P, Schulman H. Sensitivity of CaM kinase II to the frequency of Ca^{2+}oscillations. Science. 1998;279(5348):227-30.

61. Putney JW, Jr. Calcium signaling: up, down, up, down...what's the point? Science. 1998;279(5348):191-2.

62. Blitzer RD, Connor JH, Brown GP, Wong T, Shenolikar S, Iyengar R, et al. Gating of CaMKII by cAMP-regulated protein phosphatase activity during LTP. Science. 1998;280(5371):1940-2.

63. Pharris MC, Patel NM, VanDyk TG, Bartol TM, Sejnowski TJ, Kennedy MB, et al. A multi-state model of the CaMKII dodecamer suggests a role for calmodulin in maintenance of autophosphorylation. PLoS Comput Biol. 2019;15(12):e1006941.

64. Husar A, Ordyan M, Garcia GC, Yancey JG, Saglam AS, Faeder JR, et al. MCell4 with BioNetGen: A Monte Carlo simulator of rule-based reaction-diffusion systems with Python interface. PLoS Comput Biol. 2024;20(4):e1011800.

65. Faeder JR, Blinov ML, Hlavacek WS. Rule-based modeling of biochemical systems with BioNetGen. Methods Mol Biol. 2009;500:113-67.

66. Kerr RA, Bartol TM, Kaminsky B, Dittrich M, Chang JC, Baden SB, et al. Fast Monte Carlo Simulation Methods for Biological Reaction-Diffusion Systems in Solution and on Surfaces. SIAM J Sci Comput [Internet]. 2008 Oct 13 2819163]; 30(6):[3126 p.]. Available from: http://www.ncbi.nlm.nih.gov/pubmed/20151023.
67. Tapia JJ, Saglam AS, Czech J, Kuczewski R, Bartol TM, Sejnowski TJ, et al. MCell-R: A Particle-Resolution Network-Free Spatial Modeling Framework. Methods Mol Biol. 2019;1945:203-29.
68. Sneddon MW, Faeder JR, Emonet T. Efficient modeling, simulation and coarse-graining of biological complexity with NFsim. Nat Methods. 2011;8(2):177-83.
69. Gupta S, Czech J, Kuczewski R, Bartol TM, Sejnowski TJ, Lee REC, et al. Spatial stochastic modeling with MCell and CellBlender. arXiv. 2018;arXiv:1810.00499v1 [q-bio.QM].
70. Nadkarni S, Bartol TM, Stevens CF, Sejnowski TJ, Levine H. Short-term plasticity constrains spatial organization of a hippocampal presynaptic terminal. Proc Natl Acad Sci U S A [Internet]. 2012 Sep 4 PMC3437845]; 109(36):[14657-62 pp.]. Available from: http://www.ncbi.nlm.nih.gov/pubmed/22908295.
71. Goda Y, Stevens CF. Two components of transmitter release at a central synapse. Proc Natl Acad Sci U S A. 1994;91(26):12942-6.
72. Dobrunz LE, Huang EP, Stevens CF. Very short-term plasticity in hippocampal synapses. Proc Natl Acad Sci U S A. 1997;94(26):14843-7.
73. Haas KT, Compans B, Letellier M, Bartol TM, Grillo-Bosch D, Sejnowski TJ, et al. Pre-post synaptic alignment through neuroligin-1 tunes synaptic transmission efficiency. Elife. 2018;7.
74. Vargas-Caballero M, Robinson HP. Fast and slow voltage-dependent dynamics of magnesium block in the NMDA receptor: the asymmetric trapping block model. J Neurosci. 2004;24(27):6171-80.

75. Sabatini BL, Oertner TG, Svoboda K. The life cycle of Ca^{2+}ions in dendritic spines. Neuron. 2002;33(3):439-52.

76. Racca C, Stephenson FA, Streit P, Roberts JD, Somogyi P. NMDA receptor content of synapses in stratum radiatum of the hippocampal CA1 area. J Neurosci. 2000;20(7):2512-22.

77. Goncalves J, Bartol TM, Camus C, Levet F, Menegolla AP, Sejnowski TJ, et al. Nanoscale co-organization and coactivation of AMPAR, NMDAR, and mGluR at excitatory synapses. Proc Natl Acad Sci U S A. 2020;117(25):14503-11.

78. Erondu NE, Kennedy MB. Regional distribution of type II Ca^{2+}/calmodulin-dependent protein kinase in rat brain. J Neurosci. 1985;5:3270-7.

79. Ingebritsen TS, Stewart AA, Cohen P. The protein phosphatases involved in cellular regulation. 6. Measurement of type-1 and type-2 protein phosphatases in extracts of mammalian tissues; an assessment of their physiological roles. Eur J Biochem. 1983;132(2):297-307.

80. Bradshaw JM, Kubota Y, Meyer T, Schulman H. An ultrasensitive Ca2+/calmodulin-dependent protein kinase II-protein phosphatase 1 switch facilitates specificity in postsynaptic calcium signaling. Proc Natl Acad Sci U S A. 2003;100(18):10512-7.

81. Watterson DM, Harrelson WG, Jr., Keller PM, Sharief F, Vanaman TC. Structural similarities between the Ca^{2+}-dependent regulatory proteins of 3':5'-cyclic nucleotide phosphodiesterase and actomyosin ATPase. J Biol Chem. 1976;251:4501-13.

82. Kakiuchi S, Yasuda S, Yamazaki R, Teshima Y, Kanda K, Kakiuchi R, et al. Quantitative determinations of calmodulin in the supernatant and particulate fractions of mammalian tissues. J Biochem. 1982;92(4):1041-8.

83. Shifman JM, Choi MH, Mihalas M, Mayo SL, Kennedy MB. Ca^{2+}/Calmodulin-Dependent Protein Kinase II (CaMKII) is Activated by Calmodulin with Two Bound Calciums. Proc Natl Acad Sci USA. 2006;103(38):13968-73.

84. Rellos P, Pike ACW, Niesen FH, Salah E, Lee WH, von Delft F, et al. Structure of the CaMKIIdelta /Calmodulin Complex Reveals the Molecular Mechanism of CaMKII Kinase Activation. PLoS Biol. 2010;8(7):e1000426.

85. Harnett MT, Makara JK, Spruston N, Kath WL, Magee JC. Synaptic amplification by dendritic spines enhances input cooperativity. Nature. 2012;491(7425):599-602.

86. Mainen ZF, Joerges J, Huguenard JR, Sejnowski TJ. A model of spike initiation in neocortical pyramidal neurons. Neuron. 1995;15(6):1427-39.

87. Keller DX, Franks KM, Bartol TM, Jr., Sejnowski TJ. Calmodulin activation by calcium transients in the postsynaptic density of dendritic spines. PLoS One. 2008;3(4):e2045.

88. Ascher P, Nowak L. The role of divalent cations in the*N*-methyl-D-aspartate responses of mouse central neurones in culture. J Physiol. 1988;399:247-66.

89. Kennedy MB, Bennett MK, Erondu NE. Biochemical and immunochemical evidence that the "major postsynaptic density protein" is a subunit of a calmodulin-dependent protein kinase. Proc Natl Acad Sci USA. 1983;80:7357-61.

90. Shen K, Meyer T. Dynamic control of CaMKII translocation and localization in hippocampal neurons by NMDA receptor stimulation. Science. 1999;284(5411):162-6.

91. Shen K, Teruel MN, Connor JH, Shenolikar S, Meyer T. Molecular memory by reversible translocation of calcium/calmodulin-dependent protein kinase II. Nat Neurosci. 2000;3(9):881-6.

92. Sheng M, Hoogenraad CC. The postsynaptic architecture of excitatory synapses: a more quantitative view. Annu Rev Biochem. 2007;76:823-47.

93. Lisman J, Schulman H, Cline H. The molecular basis of CaMKII function in synaptic and behavioural memory. Nat Rev Neurosci. 2002;3(3):175-90.

94. Bayer KU, De Koninck P, Leonard AS, Hell JW, Schulman H. Interaction with the NMDA receptor locks CaMKII in an active conformation. Nature. 2001;411(6839):801-5.

95. Walikonis RS, Oguni A, Khorosheva EM, Jeng C-J, Asuncion FJ, Kennedy MB. Densin-180 forms a ternary complex with the α-subunit of CaMKII and α-actinin. J Neurosci. 2001;21:423-33.

96. Carlisle HJ, Luong TN, Medina-Marino A, Schenker LT, Khorosheva EM, Indersmitten T, et al. Deletion of densin-180 results in abnormal behaviors associated with mental illness and reduces mGluR5 and DISC1 in the postsynaptic density fraction. J Neurosci. 2011;31(45):16194-207.

97. Brown GP, Blitzer RD, Connor JH, Wong T, Shenolikar S, Iyengar R, et al. Long-term potentiation induced by theta frequency stimulation is regulated by a protein phosphatase-1-operated gate. J Neurosci. 2000;20(21):7880-7.

98. Bollen M, Peti W, Ragusa MJ, Beullens M. The extended PP1 toolkit: designed to create specificity. Trends Biochem Sci. 2010;35(8):450-8.

99. Brautigan DL, Shenolikar S. Protein Serine/Threonine Phosphatases: Keys to Unlocking Regulators and Substrates. Annu Rev Biochem. 2018;87:921-64.

100. Terry-Lorenzo RT, Elliot E, Weiser DC, Prickett TD, Brautigan DL, Shenolikar S. Neurabins recruit protein phosphatase-1 and inhibitor-2 to the actin cytoskeleton. J Biol Chem. 2002;277(48):46535-43.

101. Bullock SA, Platholi J, Gjyrezi A, Heerdt PM, Tung HY, Hemmings HC, Jr. Differential regulation of protein phosphatase-1(I) by neurabin. Biochem Biophys Res Commun. 2007;358(1):140-4.

102. Hsieh-Wilson LC, Allen PB, Watanabe T, Nairn AC, Greengard P. Characterization of the neuronal targeting protein spinophilin and its interactions with protein phosphatase-1. Biochemistry. 1999;38:4365-73.

103. Ragusa MJ, Dancheck B, Critton DA, Nairn AC, Page R, Peti W. Spinophilin directs protein phosphatase 1 specificity by blocking substrate binding sites. Nat Struct Mol Biol. 2010;17(4):459-64.

104. Foley K, McKee C, Nairn AC, Xia H. Regulation of synaptic transmission and plasticity by protein phosphatase 1. J Neurosci. 2021;41:3040-50.

105. Ouimet CC, da Cruz e Silva EF, Greengard P. The alpha and gamma 1 isoforms of protein phosphatase 1 are highly and specifically concentrated in dendritic spines. Proc Natl Acad Sci U S A. 1995;92(8):3396-400.

106. Dudek SM, Bear MF. Homosynaptic long-term depression in area CA1 of hippocampus and the effects of NMDA receptor blockade. Proc Natl Acad Sci USA. 1992;89:4363-7.

107. Coussens C, Teyler TJ. Protein kinase and phosphatase activity regulate the form of synaptic plasticity expressed. Synapse. 1996;24:97-103.

108. Mulkey RM, Herron CE, Malenka RC. An essential role for protein phosphatases in hippocampal long-term depression. Science. 1993;261:1051-5.

109. Jouvanceau A, Hedou G, Potier B, Kollen M, Dutar P, Mansuy IM. Partial ihibition of PP1 alters bidirectional synaptic plasticity in the hippocampus. Eur J Neurosci. 2006;24:464-572.

110. Thomas MJ, Moody TD, Makhinson M, O'Dell TJ. Activity-dependent b-adrenergic modulation of low frequency stimulation induced LTP in the hippocampal CA1 region. Neuron. 1996;17:475-82.

111. Allen PB, Ouimet CC, Greengard P. Spinophilin, a novel protein phosphatase1 binding protein localized to dendritic spines. Proc Natl Acad Sci U S A. 1997;94:9956-61.

112. Ouimet CC, Katona I, Allen P, Freund TF, Greengard P. Cellular and subcellular distribution of spinophilin, a PP1 regulatory protein that bundles F-actin in dendritic spines. J Comp Neurol. 2004;479(4):374-88.

113. Grossman SD, Hsieh-Wilson LC, Allen PB, Nairn AC, Greengard P. The actin-binding domain of spinophilin is necessary and sufficient for targeting to dendritic spines. Neuromolecular Med. 2002;2(1):61-9.

114. Zhabotinsky AM. Bistability in the Ca(2+)/calmodulin-dependent protein kinase-phosphatase system. Biophys J. 2000;79(5):2211-21.

115. Lisman JE, Zhabotinsky AM. A model of synaptic memory: a CaMKII/PP1 switch that potentiates transmission by organizing an AMPA receptor anchoring assembly. Neuron. 2001;31(2):191-201.

116. Pi HJ, Lisman JE. Coupled phosphatase and kinase switches produce the tristability required for long-term potentiation and long-term depression. J Neurosci. 2008;28(49):13132-8.

117. Michalski PJ. The delicate bistability of CaMKII. Biophys J. 2013;105(3):794-806.

118. Michalski PJ. First demonstration of bistability in CaMKII, a memory-related kinase. Biophys J. 2014;106(6):1233-5.

119. Strogatz S, H. Nonlinear Dynamics and Chaos: With Applications To Physics, Biology, Chemistry, and Engineering. Journal of Statistical Physics. 2014;Vol. 78.

120. Li L, Stefan MI, Le Novere N. Calcium input frequency, duration and amplitude differentially modulate the relative activation of calcineurin and CaMKII. PLoS One. 2012;7(9):e43810.

121. Hopfield JJ. Kinetic proofreading: a new mechanism for reducing errors in biosynthetic processes requiring high specificity. Proc Natl Acad Sci U S A. 1974;71(10):4135-9.

122. Huang WY, Yan Q, Lin WC, Chung JK, Hansen SD, Christensen SM, et al. Phosphotyrosine-mediated LAT assembly on membranes drives kinetic bifurcation in recruitment dynamics of the Ras activator SOS. Proc Natl Acad Sci U S A. 2016;113(29):8218-23.

123. Lisman J. The CaM kinase II hypothesis for the storage of synaptic memory. Trends Neurosci. 1994;17:406-12.

124. Bayer KU, LeBel E, McDonald GL, O'Leary H, Schulman H, De Koninck P. Transition from reversible to persistent binding of CaMKII to postsynaptic sites and NR2B. J Neurosci. 2006;26(4):1164-74.

125. Opazo P, Labrecque S, Tigaret CM, Frouin A, Wiseman PW, De Koninck P, et al. CaMKII triggers the diffusional trapping of surface AMPARs through phosphorylation of stargazin. Neuron [Internet]. 2010 Jul 29; 67(2):[239-52 pp.]. Available from: http://www.ncbi.nlm.nih.gov/pubmed/20670832.

126. Blitzer RD, Wong T, Nouranifar R, Iyengar R, Landau EM. Postsynaptic cAMP pathway gates early LTP in hippocampal CA1 region. Neuron. 1995;15(6):1403-14.

127. Salter MW, Kalia LV. Src kinases: a hub for NMDA receptor regulation. Nat Rev Neurosci. 2004;5(4):317-28.

Supporting Information Captions:

Fig. S1. Presynaptic voltage, glutamate release, and postsynaptic voltage during stimulus. **A**. One example of the fifty different two epoch stimuli of 5 Hz bursts of APs that were applied to the presynaptic bouton as described in the text (Example from a single simulation initiated with seed #50, as described in the text). Each burst was comprised of 5 action potentials delivered at 50 Hz. The stimulus began at 1 sec. The two epochs were separated by 2 secs. **B**. Data from A. between 1 and 1.15 secs. **C**. Glutamate concentration in the cleft after release from single vesicles during the stimulus shown in A. **D.** Data from C between 1 and 1.15 secs. **E**. Postsynaptic membrane potentials during the single simulation initiated with seed #50. **F**. Data from E between 1 and 1.15 secs. No glutamate release occurred prior to the third bAP; two release events occurred prior to the fourth bAP; no glutamate release occurred prior to the fifth bAP. Red dashed lines between C. and E. indicate ectopic release events and their associate postsynaptic potentials. Red dashed lines between D. and F. indicate EPSPs generated by glutamate release events depicted in D.

Figure S2. Channel opening kinetics in response to the stimulus shown in Figure 5. **A.** The number of open, unblocked NMDARs is shown in green, and open, blocked NMDARs in blue. **B.** Data from A. between 1 and 1.15 s. **C.** Kinetics of opening of the single VDCC on the spine membrane. **D.** Data from C. between 1 and 1.15 s. Data are averages of 50 simulations initiated with different random seeds.

Figure S3. Ca^{2+}-bound states of free CaM during the two epoch stimulus. **A.** Free CaM0, CaM4, CaM2C and CaM2N plotted with ordinate of 300 molecules. **B.** Free CaM1N, CaM1C, CaM1C1N, CaM2C1N, and CaM1C2N plotted with ordinate of 40 molecules. Blue, no-trapping model; green, trapping model.

Figure S4. Unphosphorylated CaMKII subunits (ucamkii) and CaM species bound to them during the two epoch stimulus. A. uCaMKII and CaM species bound to them in simulations of the no-trapping model. B. uCaMKII and CaM species bound to them in simulations of the trapping model. Orange lines indicate the total CaM bound to unphosphorylated CaMKII in each model. There is no significant difference between non-trapping and trapping models in the numbers of CaM species bound to uCaMKII during the stimulus.

Figure S5. Binding of PP1 to pCaMKII subunits in simulations of the trapping model, in the absence of competition with CaM binding. **A.** PP1 bound to CaMKII. **B.** Free PP1.

Blue, 0.65 μM PP1; Green, 1.25 μM PP1; Gold, 2.5 μM PP1.